Fall 2014

Transport studies of reentrant integer quantum Hall states forming in the two-dimensional electron gas

Nianpei Deng
Purdue University

PURDUE UNIVERSITY
GRADUATE SCHOOL
Thesis/Dissertation Acceptance

This is to certify that the thesis/dissertation prepared

By Nianpei Deng

Entitled
Transport Studies of Reentrant Integer Quantum Hall States Forming in the Two Dimensional Electron Gas

For the degree of   Doctor of Philosophy

Is approved by the final examining committee:

Gabor Csathy

Michael Manfra

Adam Wasserman

Leonid Rokhinson

To the best of my knowledge and as understood by the student in the Thesis/Dissertation Agreement, Publication Delay, and Certification/Disclaimer (Graduate School Form 32), this thesis/dissertation adheres to the provisions of Purdue University's "Policy on Integrity in Research" and the use of copyrighted material.

Gabor Csathy

Approved by Major Professor(s): _____

_____

Approved by: Mark Haugan   11/25/2014

Head of the Department Graduate Program   Date

TRANSPORT STUDIES OF REENTRANT INTEGER QUANTUM HALL

STATES FORMING IN THE TWO-DIMENSIONAL ELECTRON GAS

A Dissertation

Submitted to the Faculty

of

Purdue University

by

Nianpei Deng

In Partial Fulfillment of the

Requirements for the Degree

of

Doctor of Philosophy

December 2014

Purdue University

West Lafayette, Indiana

ACKNOWLEDGMENTS

I would like to express my deepest appreciation to my advisor, Professor Gábor Csáthy, who encourages me to work hard to achieve a set of goals in my research. I want to thank him for his patience on my slow learning of all experimental techniques and also the enlightening comments to help me improve my English writing skills.

I would like to thank my committees, Professors Adam Wasserman, Leonid Rokhinson and Michael Manfra who spent time to review my dissertation and to give me useful advice.

In addition, I would like to thank my collaborators at both Purdue University and Princeton University. Without the exceptionally high quality samples grown by Professor Michael Manfra, John Watson and Geoff Garder at Purdue Univeristy as well as Loren Pfeiffer and Kenneth West at Princeton University, we cannot measure any of those beautiful traces. I want to especially thank Professor Leonid Rokhinson for the valuable discussions on reentrant integer quantum Hall states which helped me continue this project.

Last but not least, I want to thank my colleagues Ashwani Kumar, Nodar Samkharadze, Ethan Kleinbaum and Ian Arnold. From everyday discussions with them in the lab, I keep learning outside my field of research. I also want to thank my wife Jing Dong for supporting me in writing this dissertation.

TABLE OF CONTENTS

LIST OF TABLES

LIST OF FIGURES

Figure Page

Figure   Page

ABSTRACT

Deng, Nianpei. Ph.D., Purdue University, December 2014. Transport Studies of Reentrant Integer Quantum Hall States Forming in The Two-dimensional Electron Gas. Major Professor: Gábor A. Csáthy.

The two dimensional electron gas subjected to a magnetic field has been a model system in contemporary condensed matter physics which generated many beautiful experiments as well as novel fundamental concepts. These novel concepts are of broad interests and have benefited other fields of research. For example, the observations of conventional odd-denominator fractional quantum Hall states have enriched many-body physics with important concepts such as fractional statistics and composite fermions. The subsequent discovery of the enigmatic even-denominator $\nu = 5/2$ fractional quantum Hall state has led to more interesting concepts such as non-Abelian statistics and pairing of composite fermions which can be intimately connected to the electron pairing in superconductivity. Moreover, the observations of stripe phases and reentrant integer quantum Hall states have stimulated research on exotic electron solids which have more intricate structures than the Wigner Crystal.

In contrast to fractional quantum Hall states and stripes phases, the reentrant integer quantum Hall states are very little studied and their ground states are the least understood. There is a lack of basic information such as exact filling factors, temperature dependence and energy scales for the reentrant integer quantum Hall states. A critical experimental condition in acquiring this information is a stable ultra-low temperature environment. In the first part of this dissertation, I will discuss our unique setup of ^{3}He immersion cell in a state-of-art dilution refrigerator which achieves the required stability of ultra-low temperature. With this experimental setup, we are able to observe for the first time very sharp magnetotransport features of reentrant integer quantum Hall states across many Landau levels for the first time. I will firstly present

our results in the second Landau level. The temperature dependence measurements reveal a surprisingly sharp peak signature that is unique to the reentrant integer quantum Hall states. Such a peak signature allows us to define the energy scale of reentrant integer quantum Hall state. An analysis of the energy scales indicate the collective nature of electron solid states. In the following I will present our results in the third Landau level and higher Landau levels which are used in testing the bubble theory predictions for the reentrant integer quantum Hall states. Currently there is no direct experimental probe of the microscopic structures of the reentrant integer quantum Hall states. Instead, by contrasting their energy scales, we find that certain predictions of the bubble theory are at odds with experimental data in the low Landau level limit. Furthermore, an orbital dependent energy scale from the second Landau level to the fifth Landau level is found which will provide useful insights in determining the bubble structures of these reentrant integer quantum Hall states.

It must be appreciated that the reentrant integer quantum Hall states have only been observed in the cleanest GaAs/AlGaAs samples. While the highest electron mobility has been achieved in this system by Molecular Beam Epitaxy technique, further improvements are still necessary to facilitate the study of fragile many-body ground states. However, it is little understood that how different disorder which limits the electron mobility affects the strength of the many-body ground states. In the second part of this dissertation, I will present our work on the impact of alloy disorder on the $\nu = 5/2$ fractional quantum Hall state. This work is conducted in a series of specially engineered GaAs/AlGaAs samples with controllable alloy disorder. We are able to quantitatively measure the suppression of the $\nu = 5/2$ fractional quantum Hall state by alloy disorder scattering. Surprisingly, the $\nu = 5/2$ state is found to develop at significantly reduced mobility compared with the empirical mobility threshold according to prior experiments. An analysis of the results indicates that the short-range alloy disorder and the long-range Coulomb disorder play different roles in the formation of the $\nu = 5/2$ fractional quantum Hall state.

1. INTRODUCTION TO THE GROUND STATES OF THE TWO DIMENSIONAL ELECTRON GAS

The two dimensional electron gas (2DEG) subjected to a magnetic field has been a fascinating system which exhibits astonishingly rich ground states that embody important physics concepts. In 1980, Klaus von Klitzing and his collaborators discovered the integer quantum Hall effect in a 2DEG confined to a silicon field effect transistor [1]. As shown in Fig 1.1 the Hall resistance displayed a series of plateaus of values quantized exactly to:

$$R_{xy} = h/Ne^2 = R_K/N; N = 1, 2, 3, \ldots \tag{1.1}$$

The exact quantization of R_{xy} allows a precise measurement of the R_K called the von Klitzing constant. Quite remarkably the R_K constant relates to the fine-structure constant $\alpha = \mu_0 c/2R_K$ from quantum electrodynamics to an accuracy of 3×10^{-7} [2]. The von Klitzing constant is adopted as a resistance standard in metrology. The exact quantization of Hall plateaus of the integer quantum Hall effect is a consequence of a gapped energy spectrum of single electron (Landau levels) and disorder induced single electron localization known as Anderson localization.

In 1982, D.C. Tsui, H.L. Stormer, and A.C. Gossard observed a similar Hall plateau but quantized at $R_{xy} = h/(\frac{1}{3}e^2)$ in a 2DEG confined to a GaAs/AlGaAs heterostructure (see Fig 1.2) [3]. The newly emerged Hall plateau corresponds to the fractional quantum Hall effect (FQHE) whose underlying physics completely differs from that of the integer quantum Hall effect. Since the $\nu = 1/3$ FQHE cannot be explained by the single electron physics, it aroused instantly the theoretical interest in searching for many-body solutions in which electron-electron Coulomb interaction is taken into account. R.B. Laughlin firstly described the ground state of the $\nu = 1/3$ FQHE with a particular many-body wavefunction and found its elementary excitation
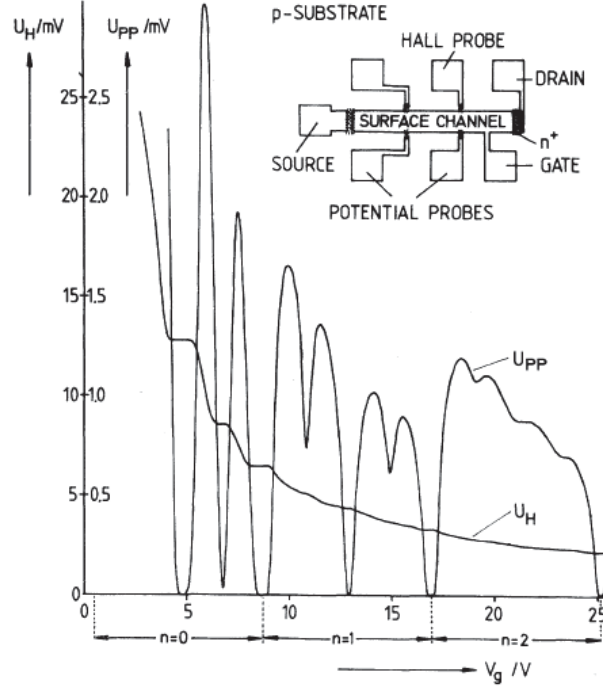
Figure 1.1. Magnetotransport data measured by Klaus von Klitzing in a silicon MOSFET. The integer quantum Hall effect corresponds to plateaus in Hall resistance U_H and zero longitudinal resistance U_{PP}. The magnetic field was fixed while the gate voltage linearly changes the electron density. Picture is taken from Ref. [1]

to be fractionally charged [4]. As more FQHEs at other fractions were discovered in experiments, J.K. Jain proposed a different approach known as composite fermion approach to account for a whole class of FQHE [5]. The existence of composite fermion was further supported by numerous experiments and its many properties such as effective mass, spin can be measured [7].

The discovery of $\nu = 5/2$ FQHE further complicates the physics of 2DEG since the $\nu = 5/2$ FQHE does not belong to the conventional class of FQHE that originates from the composite fermion approach [8]. Intensive theoretical study of the ground state of $\nu = 5/2$ FQHE has given rise to many profound concepts such as paired composite fermions with Pfaffian correlations, non-Abelian quasiparticles [9–18] and topologically protected quantum computing [19]. However, verifications of these con-
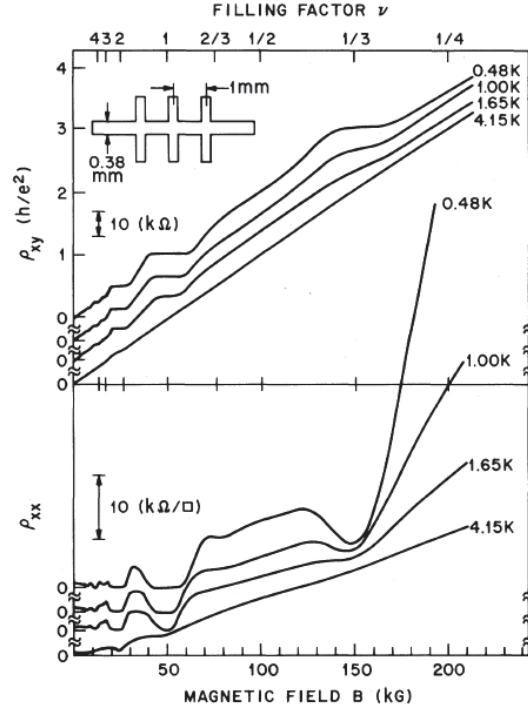
Figure 1.2. Hall resistance ρ_{xy} and longitudinal resistance ρ_{xx} taken by D.C. Tsui et al. at different temperature. The $\nu = 1/3$ FQHE can be clearly observed around a magnetic field of 150kG. The Picture is taken from Ref. [3]

cepts are difficult tasks for experiments and research on the $\nu = 5/2$ FQHE remains very active.

While the ground states of integer quantum Hall effect, conventional and exotic FQHE bear the general characteristics of a quantum liquid, a set of electronic solids can also form in the 2DEG and receive wide interests. A typical example of electron solids is the two dimensional Wigner Crystal formed at extremely high magnetic fields [21]. Such a periodic ground state is simply stabilized by strong Coulomb interaction between electrons. In relatively weak magnetic fields, more intricate electrons solids such as stripe phase and bubble phase [22] can form and are believed to result in peculiar transport phenomena, namely anisotropic resistivity and reentrant integer quantum Hall effect [23–25]. Among these transport phenomena, the reentrant

integer quantum Hall effect has only been observed in GaAs/AlGaAs quantum well structures. Strong phase competitions between the reentrant integer quantum Hall effect with both stripe phase and FQHE render it a very attractive correlated ground state to study.

In the following, a detailed introduction of creating quantum well in device as well as 2DEG confinement is given in section 1.1; A theoretical background of the physics of single electron subjected to a magnetic field is given in section 1.2; A review of the theory on two dimensional electron solids in weak magnetic fields is given in section 1.3; A history of experimental study of electron solids is given in section 1.4; A brief review of the composite fermion theory for the conventional FQHEs is given in section 1.5; A review of both experimental discoveries and theoretical research on $\nu = 5/2$ FQHE is given in section 1.6; A discussion of GaAs/AlGaAs system in engineering the cutting-edge 2DEG devices is given in section 1.7; Finally, an outline of the body of this dissertation is given in section 1.8.

1.1 Confining An Electron Gas To A Quantum Well

The confinement of an electron gas to two dimensions is achieved by band engineering. The first step of band engineering is to draw the band diagram of the designed device structures composed of different materials. Since we only consider the lowest energy state in each material, the complex band structure can be simplified with only two energies: one at the conduction band edge E_c and the other at the valence band edge E_v. The energy difference $E_c - E_v$ is equal to the band gap E_g. Moreover, each material has a corresponding vacuum level. The vacuum level is associated with the electron affinity χ which measures the energy required to excite an electron from the conduction band to the vacuum level.

For one kind of charge neutral crystal material, the band diagram can be represented by three horizontal lines: two at E_c and E_v and one at the vacuum level.
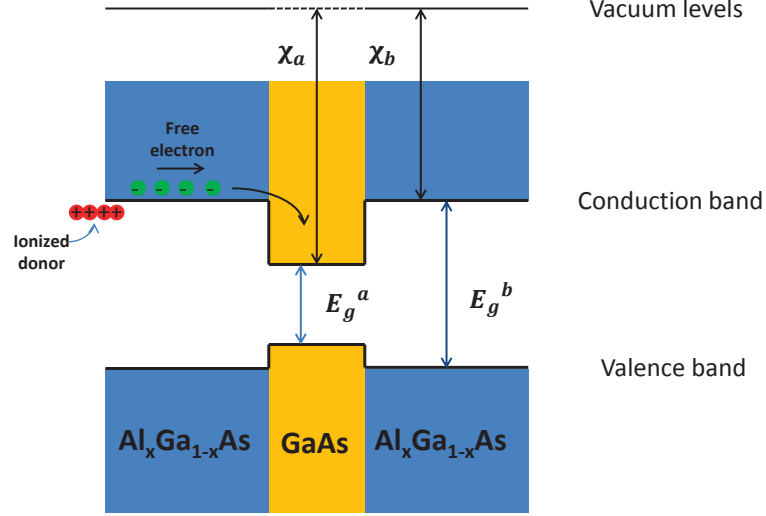
Figure 1.3. The band diagram of a sandwich structure $Al_xGa_{1-x}As/GaAs/Al_xGa_{1-x}As$. The conduction band, valence band and vacuum level are marked aside. E_g stands for the band gap and χ is the electron affinity. The donor atoms as well as the excited electrons are also drawn to demonstrate the modulation doping scheme.

When joining two different materials, the whole band diagram can be obtained by aligning their vacuum levels according to Anderson's rule [2]. As a consequence, the band diagram may have a discontinuity in both E_c and E_v at the interface.

In the experiments described in this dissertation, all devices contain a sandwich structure consisting of two materials: GaAs and $Al_xGa_{1-x}As$. The latter is an intermediate alloy between GaAs and AlAs. The physical properties of $Al_xGa_{1-x}As$ such as lattice constant and bang gap can be approximated by linear interpolation between that of the GaAs and AlAs. At a typical value of $x = 0.3$, such an alloy has a band gap of 1.8eV which is larger than the band gap of 1.4eV in GaAs. Fig 1.3 sketches the band diagram of this device structure $Al_xGa_{1-x}As/GaAs/Al_xGa_{1-x}As$. Since the χ of GaAs and $Al_xGa_{1-x}As$ is 4.07eV and 3.74eV respectively, we can calculate the

discontinuity in the conduction band to be 0.33eV. Therefore, a quantum well of a height of 0.33eV is achieved in this device to confine the electrons in the direction perpendicular to the interface.
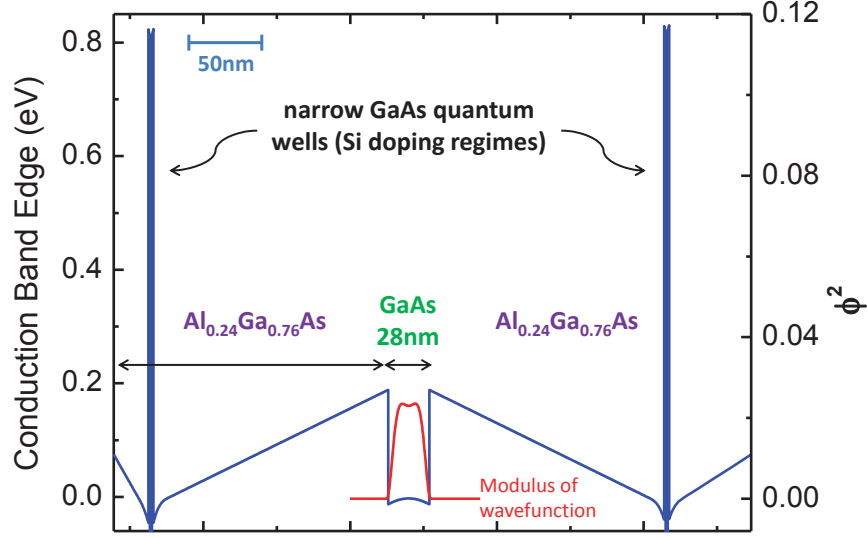
Figure 1.4. A simulated band diagram of an actual device using software NextNano3. Only the conduction band is shown here by the blue curve. In this device the silicon doping layers are grown at both sides of the quantum well. The silicon doping is achieved by short-period superlattice doping scheme. The modulus of the electron wavefunction of the lowest subband in the quantum well is shown by the red curve.

The next step is to introduce the electrons into the quantum well. Instead of placing Si donors directly into the quantum well, they are placed away from the quantum well in a small region in $Al_xGa_{1-x}As$. As indicated by the schematics in Fig 1.3, the excited electrons can then migrate to the quantum well and get trapped. This doping scheme is called the modulation doping as the electrons are separated from the donors [103]. A non-zero spatial charge distribution due to the ionized donors and trapped electrons can modify the band diagram. A self-consistent simulation

including both Si doping layers as well as electron gas in the quantum well is shown in Fig 1.4 for a typical device used in experiments. In addition, the wavefunction of the lowest energy subband of the quantum well is also shown in Fig 1.4, from which we can see that electrons are mostly situated in the middle of the quantum well.

1.2 The Two Dimensional Electron Gas Subjected To A Magnetic Field
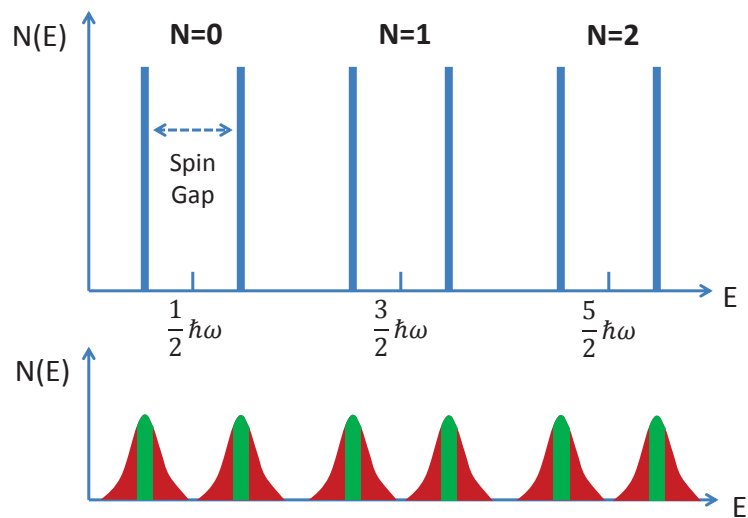
Figure 1.5. The density of states for an electron confined to two dimensions and subjected to a magnetic field. The upper plots shows the density of states of a clean 2DEG where thick lines represent δ-functions. Each Landau level numbered by N has two spin branches separated by the spin gap. The lower plot shows the disorder induced broadening of the density of states. The green part in the middle of each density of states represents the extended electron states whereas the red parts at both tails are the localized states.

When the interface of a heterostructure is subjected to a magnetic field, the kinetic energy of an electron confined to two dimensions becomes quantized at discrete energy levels:

$$E_N = (N + 1/2)\hbar\omega; N = 0, 1, 2, \ldots \tag{1.2}$$

These energy levels are called Landau levels with N=0 referring to the lowest Landau level, N=1 referring to the second Landau level and so on. When this system has an area of S, the number of states in each Landau level shares the same value expressed as:

$$2eBS/h \tag{1.3}$$

Number 2 in the expression represents the spin degeneracy. The perpendicular magnetic field lifts the spin degeneracy and breaks the two dimensional density of states into a sequence of δ-functions as shown in the sketch of Fig 1.5. By considering a 2DEG of density n in a unit area, the filling fraction of Landau levels can be derived as:

$$\nu = nh/eB \tag{1.4}$$

The integer part of ν indicates the number of filled Landau levels whereas $\nu^* = \nu - [\nu]$ indicates the partial filling fraction of the topmost Landau level. In real systems, the scattering of electron by disorder or other mechanisms is inevitable and the δ-function density of states is consequently broadened with a width of Γ. Disorder not only causes the broadening of the energy levels of electron but also induces localization of many of the states in a Landau level (as shown in Fig 1.5). Such a localization caused by random potential disorder is called Anderson localization [26]. Since a localized state does not contribute to the currents, it is of great importance in explaining the existence of quantized Hall plateaus in the integer quantum Hall effect.

Another important concept in the 2DEG subjected to a magnetic field is the edge state. For convenience, the Landau gauge is adopted and the electron wavefunction is solved as:

$$\phi_{nk} = H_{n-1}\left(\frac{x - x_k}{l_B}\right) exp\left(-\frac{(x - x_k)^2}{2l_B^2}\right) exp(iky); x_k = -\hbar k/eB \tag{1.5}$$
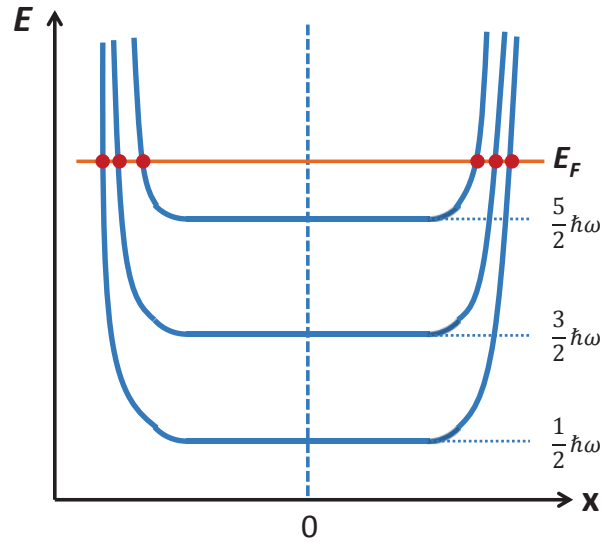
Figure 1.6. The bending of Landau levels as a function of the position in x direction. The bending in x direction is caused by confinement potential and the dash line represents the center in x direction. The red dots at the crossing of Fermi level and energy levels represent edge states.

Here the H_n are Hermite polynomials. Such a wavefunction describes an electron traveling in y direction with a momentum of $\hbar k$ but localized at x_k in the x direction. While the electron density is uniform in the bulk, it gradually becomes depleted at the edges so that the density gradient can create a large confining potential in the x direction shown in Fig 1.6. The electronic potential is hence flat in the bulk but increases rapidly at the edges. When the Fermi energy level lies between Landau levels, the two crossings of it with each energy band correspond to the edge states. The two edge states in each energy band are current carrying states with opposite momenta. Due to the space separation, no back scattering will occur in the transport of the edge states. Such a property of edge state results in a vanishing longitudinal resistance in the integer quantum Hall effect.

1.3 The Theory Of Two Dimensional Electron Solids In Weak Magnetic Fields

In a weak magnetic field, the two dimensional electron solids (or strictly speaking charge density waves) were firstly predicted by a Hartree-Fock study in 1996 [22]. In this study, three types of electron solids, i.e. stripe phases, bubble phases and Wigner Crystal were found as the ground states in different filling factors. Subsequent magnetotransport measurements in a 2DEG in 1999 indeed revealed new transport features such as anisotropic resistivity and reentrant integer quantum Hall effect which could be understood based on the predicted electron solids [23, 24]. The Hartree-Fock theory of two dimensional electron solids is hence one of the few examples to successfully predict many-body ground states in the two dimensional electron gas.

Stripe phase   Bubble phase   Wigner Crystal
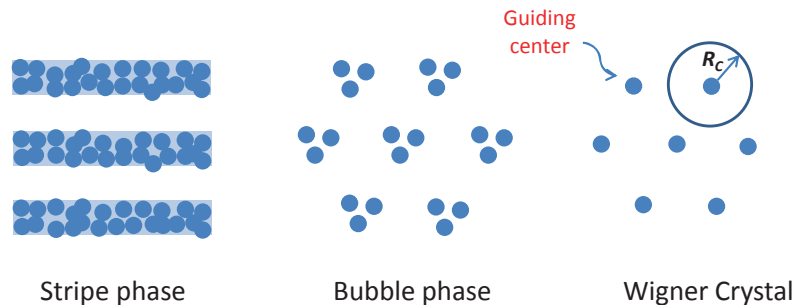
Figure 1.7. The schematic drawing of the crystal pattern of three types of electron solids predicted in the 2DEG. Each dot represents the guiding center of an orbiting electron of radius R_C. The stripes represent a uniform distribution of electrons.

In a classical three dimensional crystal, each atom or molecule is arranged in a position specified by fixed coordinates. In contrast, the two dimensional electron solids subjected to a magnetic field consists of orbiting electrons whose individual position can only be described by a wavefunction. In particular, the wavefunction of electrons in the topmost Landau level has a ringlike shape with a radius of R_c as shown in Fig 1.7. R_c is the cyclotron radius defined as $\hbar k_F / eB$ where k_F is the

Fermi wave vector of the 2DEG. Such a wavefunction description of electron makes it difficult to describe the electron solids with the location of electron itself. Instead, the guiding center of the electron orbit is treated as the classical object in describing the crystal order. A unique feature of the electron solids is that while their guiding centers form a crystal, the actual charge density can have a relatively uniform distribution. Such a distribution of charge density in turn lowers the Hartree energy.

The essential idea of Hartree-Fock theory is to minimize the energy for a many-body wavefunction with variable parameters. In the study of two dimensional electron solids, the guiding center density is the designated parameter function. The results of the guiding center density function turn out to exhibit three types of crystal patterns as shown in Fig 1.7 [22]. Here, we only consider the electrons in the partially filled topmost Landau levels by using the partial filling factor ν^*. The remaining electrons in the N filled Landau levels are considered inert. At ν^* close to 0.5, the high density of electrons results in a large overlap between adjacent electron orbits, and the pattern is an alternation between uniform electron stripes and empty stripes. At $\nu^* << 1/N$, the electrons are quite sparse, and the pattern is a Wigner crystal with only one electron in each unit cell. At ν^* between above two limits, the electrons form a new crystal (named bubble phase) similar to the Wigner crystal but with more than one electron condensing into each unit cell. The cases of $\nu^* > 0.5$ can be related to that of $1 - \nu^*$ by particle-hole symmetry. One important distinction between the stripe phase and bubble phase as well as Wigner crystal is that the first one is anisotropic while the latter two are isotropic.

The Hartree-Fock theory is not the only one to predict the formation of two dimensional electron solids. Following works by numerical methods including exact diagonalization [27] and density matrix renormalization group [28] also support the existence of stripe phases and bubble phases in the third Landau level and even higher ones. Moreover, the Hartree-Fock theory has been extended to the regime of relatively high magnetic fields where the second Landau level is occupied [29]. The reentrant

integer quantum Hall effect in the second Landau level, however, is quite different than those in the higher Landau levels and remains to be an interesting topic.

1.4 Transport Signatures Of Electron Solids Discovered In Experiments
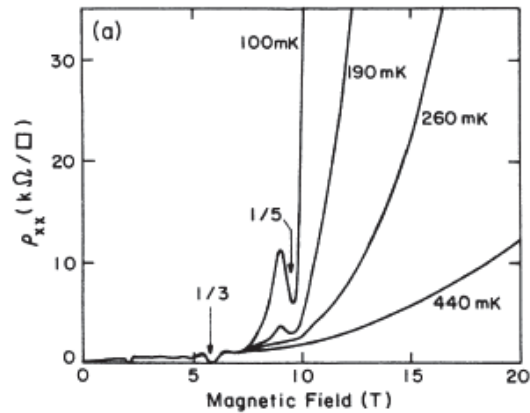
Figure 1.8. Longitudinal resistivity measured in the lowest Landau level by R.L. Willet et al. At magnetic fields higher than the $\nu = 1/5$ fractional quantum Hall effect, the resistivity increases rapidly with lowering temperature. Such an insulating behavior is interpreted as the formation of magnetically induced Wigner crystal. Picture is taken from Ref. [20]

The Wigner crystal is the earliest electron solid believed to form in a two dimensional electron gas subjected to magnetic fields [21]. As shown in Fig 1.8, at magnetic fields beyond the $\nu = 1/5$ FQHE, the resistivity is large and increases with lowering temperature [20]. The insulating behavior at such high magnetic fields can be explained by the localization of the magnetically induced Wigner crystal. Due to the strong magnetic field, each electron can be confined to an area of h/eB which is occupied by a single magnetic flux. Therefore, the filling factor $\nu = nh/eB$ indicates the ratio of the dimension of magnetically induced confinement to the average inter-electron distance. At small ν and high magnetic fields, such a confinement is much smaller than the inter-electron distance and the Coulomb interaction is able to

stabilize the spatial crystal order of the 2DEG. In experiments, evidences of gapless magnetophonon excitation as well as an electric-field threshold conduction were found to support the existence of Wigner crystal in the limit of high magnetic fields [21].
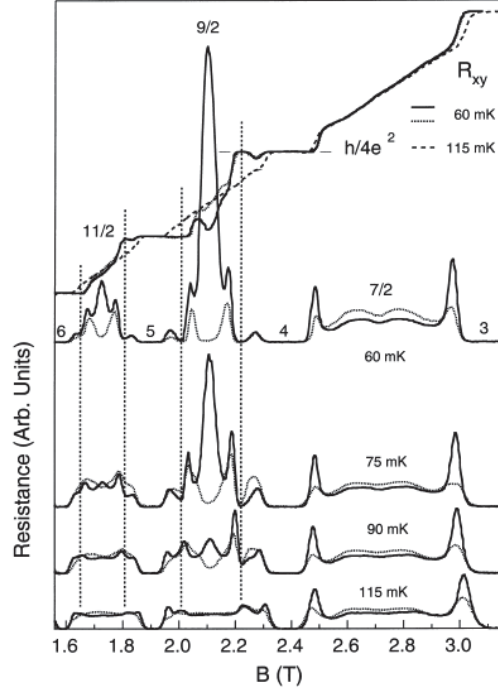
Figure 1.9. Original data of stripe phase and reentrant integer quantum Hall effect from R.R. Du et al. The largely anisotropic stripe phases can be identified at $\nu = 9/2$ and $\nu = 11/2$ in the third Landau level. The reentrant integer quantum Hall effect showed up at the vertical dotted lines. Picture is taken from Ref. [24]

In weak magnetic fields, the first evidence of electron solids was found in the magnetotransport measurements by two different groups [23, 24]. From the data shown in Fig 1.9 [24], two prominent features can be observed in the third Landau level of filling factor range $4 < \nu < 6$. The first one is the large anisotropy in the longitudinal resistances R_{xx} at $\nu = 9/2$ and $\nu = 11/2$. The solid and dotted lines were measured in mutually perpendicular directions or specifically crystalline axes [110] and [1$\bar{1}$0]. The R_{xx} reaches a large maximum in one direction but vanishes in the other direction. Such a feature is attributed to the formation of stripe phases

at $\nu = 9/2$ and $\nu = 11/2$ such that the 2DEG can easily conduct in the same direction of the stripes but hardly conduct in perpendicular direction to the stripes. The underlying origin of the hard conducting direction is a pinning of stripe phases by random disorder potentials. The second one is four emergent new Hall plateaus at four vertical dotted lines drawn in Fig 1.9. These features were called reentrant integer quantum Hall effect because the new Hall plateaus are separate from those of the integer quantum Hall effect. Regardless of the direction of the measurements, the regions of the reentrant integer quantum Hall effect look the same indicating that they correspond to isotropic ground states. It has been widely believed that bubble phases form in the reentrant regions. The discoveries of both stripe phases and reentrant integer quantum Hall effect were not limited to the third Landau level. In fact, depending on the quality of the 2DEG, these two effects can persist to very high Landau levels.

More surprisingly, the reentrant integer quantum Hall effect was also discovered in the second Landau level in 2002 [25]. One important difference between reentrant integer quantum Hall effect in the second Landau level and that in higher Landau levels is the number of reentrant integer quantum Hall effect. There are four reentrant integer quantum Hall effects developing in each spin branch of the second Landau level whereas there are only two reentrant integer quantum Hall effects developing in each spin branch of higher Landau level (see Fig 1.10). According to the Hartree-Fock theory, the reentrant integer quantum Hall effect in the second Landau level are associated with two types of bubble phases: one-electron bubble phase and two-electron bubble phase [29].

As shown in Fig 1.10, when the filling factor is close to $\nu = 3$, the integer quantum Hall effect occurs where electrons are randomly distributed and localized individually. However, increasing the filling factor leads to the formation of the one-electron bubble phase which is localized collectively due to a pinning by disorder potential. Therefore, the bubble phases result in an insulating state in the bulk. Only the two edge states can still contribute to the current flow and the Hall resistance remains the same as
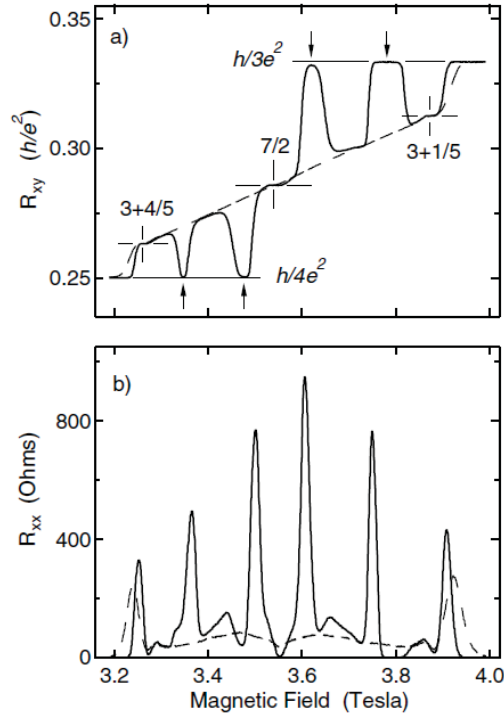
Figure 1.10. The discovery of reentrant integer quantum Hall effect in the second Landau level from J.P. Eisenstein et al. In this plot the upper spin branch of the second Landau level is shown and four reentrant integer quantum Hall effects can be observed. Picture is taken from Ref. [25]

that of the integer quantum Hall effect. At even higher filling factor, the electrons in the topmost Landau level become more dense and they form the two-electron bubble phase. The corresponding Hall features can be explained by the same reasoning for the one-electron bubble phase.

The magnetotransport measurement is not the only experimental study of reentrant integer quantum Hall effect and stripe phase. It must be acknowledged that other techniques such as nonlinear I-V characteristics, surface acoustic wave, microwave resonances have been applied to their studies [30–33]. Among these techniques, the microwave resonance has been very powerful in probing the collective pinning mode of the reentrant integer quantum Hall effect. However, so far none of these experiments are able to probe the microscopic structures of the bubble phases.
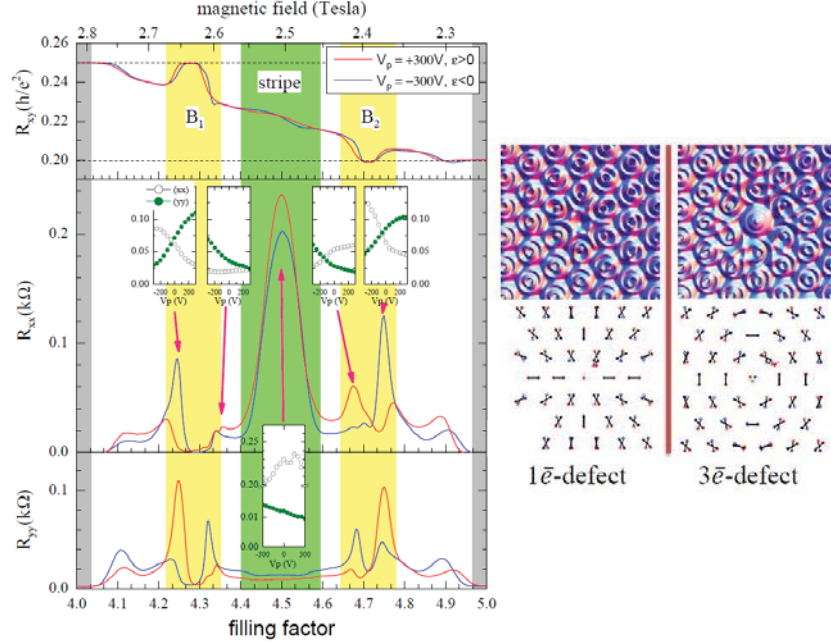
Figure 1.11. On the left is the strain dependent resistivity measured in the reentrant integer quantum Hall effect in the third Landau level. On the right are the topological textures around two different charge defects which are predicted to cause such a strain dependent resistivity of reentrant integer quantum Hall effect. Picture is taken from Ref. [34]

Very recently, the strain effects have been investigated in the reentrant integer quantum Hall effect in the third Landau level which reveal intriguing results on other aspects of the bubble phases [34]. As seen in the Fig 1.11, the two resistivity peaks at the boundary of each reentrant integer quantum Hall effect demonstrate very different strain dependence. This experimental observation is explained by topologically non-trivial textures which form around different charge defects. Such a theory of topological defects is likely of great importance in understanding the peculiar temperature dependence of the reentrant integer quantum Hall effect.

Despite these experimental efforts devoted to the study of RIQHE, many important properties of RIQHE such as exact filling factors, temperature behaviors or energy scales are still unknown. Furthermore, the reentrant integer quantum Hall

effect in the SLL requires stringent experimental conditions like low temperature to develop and very few data has been taken in this region. These topics hence become the focus of part of this dissertation.

1.5 The Composite Fermion Theory

A powerful approach to account for the conventional fractional quantum Hall effects is the weakly interacting composite fermion theory [6]. This approach is able to map the fractional quantum Hall effect to the integer quantum Hall effect by a flux attachment scheme. By binding each electron with a even number of flux quanta h/e, a new particle called composite fermion is used to describe the 2DEG. In analogy with the integer quantum Hall effect, the composite fermions occupy a set of new Landau level and the filling fraction is ν'. The actual electron filling fraction ν can be related to ν' by equation:

$$\nu = \nu'/(2p\nu' + 1) \tag{1.6}$$

where 2p is the number of flux quanta being attached. When ν' is an integer, it corresponds to the fractional quantum Hall effect at ν of odd-denominator. For example, the $\nu = 1/3$ fractional quantum Hall effect can be explained by the $\nu' = 1$ integer quantum Hall effect of 2-flux composite fermions. The 2-flux composite fermions can be considered weakly interacting particles and experience a reduced effective field of $B_{eff} = B - 2nh/e$ with n being the density of the 2DEG. When $B = 2nh/e$ or $\nu = 1/2$, the effective field is zero and the ground state corresponds to a fermion sea of composite particles. Indeed, this composite fermion sea has been confirmed in experiments [6].

1.6 The $\nu = 5/2$ Fractional Quantum Hall Effect

While the weakly interacting composite fermion theory has achieved great success in constructing the hierarchy of odd-denominator FQHEs, the existence of even-denominator $\nu = 5/2$ FQHE becomes a direct violation of this theory. The composite

fermion theory expects a composite fermion sea at $\nu = 5/2$ which is similar to what has been observed at $\nu = 1/2$. However, R. Willett et al. discovered an incipient FQHE at $\nu = 5/2$ in 1987 as shown in Fig 1.12 [8]. The realization of an exactly quantized Hall plateaus at $\nu = 5/2$ was achieved by W. Pan et al. twelve years later to corroborate the existence of $\nu = 5/2$ FQHE [35].
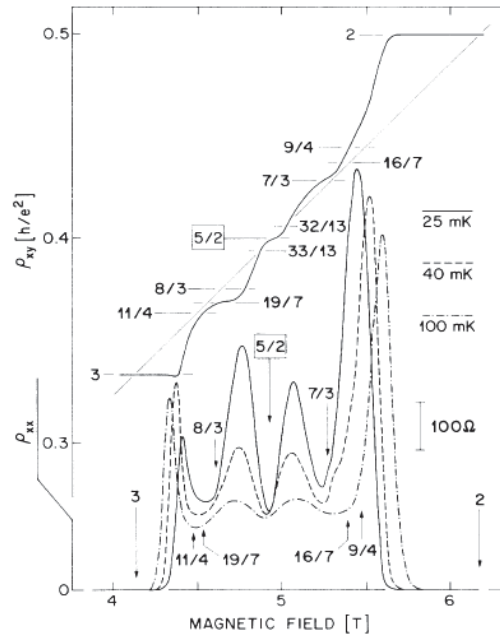
Figure 1.12. Observation of $\nu = 5/2$ FQHE by R. Willett et al. It was noted that although a dip appears at $\nu = 5/2$, it did not develop further with decreasing temperature. Picture is taken from Ref. [8]

The Moore-Read Pfaffian wavefunction is believed to be the most prominent candidate in describing the ground state at $\nu = 5/2$ [9]. The Pfaffian wavefunction has intimate connection with the wavefunction of spin-polarized p-wave BCS superconductivity. It was found that in the medium of electrons of the two fully filled Landau levels, the 2-flux composite fermions in the topmost Landau level can form a stable pair state [15]. Due to the pairing of composite fermions, a gapped energy spectrum appears instead of a continuous energy spectrum of composite fermion sea. It is noted

that the pairing mechanism of composite fermions is different than the phonon mediated pairing of electrons in superconductivity. Such a composite fermion pairing is an intrinsic property of strongly interacting 2DEG in magnetic field.

The Moore-Read Pfaffian wavefunction itself is a very interesting topic which has attracted considerable theoretical attentions [10–18]. One important property of this wavefunction is that the quasi-particles from the excitations of its ground state obey non-abelian statistics. This is fundamentally different than the fractional statistics of the quasi-particles in the conventional FQHEs. In fractional statistics, the interchange of two particles only results in a change of phase factor in the wavefunction. However, in non-abelian statistics, the interchange of two particles leads to a new wavefunction. The corresponding interchange can be regarded as a non-commutable matrix operation. The non-abelian property of Moore-Read Pfaffian wavefunction can be further utilized in a fault-tolerant topological quantum computation [19].

One important thing to mention is that it is very difficult to prepare a fully quantized $\nu = 5/2$ FQHE in experiments. Due to a small energy gap, one has to fabricate a high quality device and to cool the device to very low electron temperature (under 100mK). Although the theories predict an intrinsic energy gap of order of Kelvins, the largest experimental value is only around 600 mK [36]. The reduction of energy gap is mostly caused by disorder broadening of the energy levels. Therefore, in order to increase the energy gap of $\nu = 5/2$ FQHE and to then facilitate subsequent experiments, the disorder effects on $\nu = 5/2$ FQHE need to be elucidated.

1.7 Advantages Of The GaAs/AlGaAs System In Two Dimensional Electron Physics

The progress of discovering new ground states in the 2DEG is paralleled by continuous improvements of its host devices. A key parameter in measuring the quality of
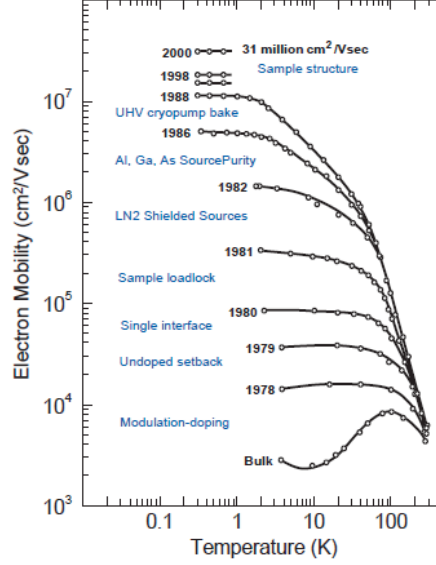
Figure 1.13. History of the developments in the Molecular Beam Epitaxy technique by L.N. Pfeiffer and K.W. West. The continuous developments of MBE technique almost increased electron mobility by a factor of 10^4 over the years. Picture is taken from Ref. [37]

the device is the electron mobility μ. The electron mobility is related to the transport scattering time τ by expression:

$$\mu = \frac{e\tau}{m^*} \tag{1.7}$$

where m^* is the effective mass of electron. The mobility has a strong temperature dependence due to temperature dependent phonon scattering rate but tends to saturate at low temperature when phonons freeze out. Therefore we usually refer to the low temperature mobility of the devices in studying 2DEG ground states.

The original device in which integer quantum Hall effect was discovered is a silicon field effect transistor with an electron mobility limited to $10\text{cm}^2/\text{Vs}$. The interface roughness between Si and amorphous SiO_2 can cause strong scattering of electrons which severely limits the electron mobility. By comparison, the observation of fractional quantum Hall effect was achieved in a GaAs/AlGaAs heterostructure of which the electron mobility reached $100\text{cm}^2/\text{Vs}$. Because the lattice constant of crystal GaAs and AlAs differs less than 0.15%, layers of GaAs can be grown onto any inter-

mediate alloy $Al_xGa_{1-x}As$ and the resultant interface is much cleaner to confine the 2DEG. Moreover, the free moving electron gas is introduced to the confinements by modulation doping. One benefit of this doping scheme is that the electrons migrate away from the ionized donors which further reduces the scattering due to ionized impurities.

In order to engineer such a heterostructure, a sophisticated technique called Molecular Beam Epitaxy is used to grow the desired structures with a precision of one mono-layer of atoms [38]. Fig 1.13 recorded a series of developments to the Molecular Beam Epitaxy technique which lead to significant increase of electron mobility [37]. As electron mobility of the device increased, more fragile fractional quantum Hall effects such as $\nu = 5/2$ fractional quantum Hall effect and reentrant integer quantum Hall effect were discovered. Samples used in this dissertation have mobility over $10^7 cm^2/Vs$ in order to observe more robust $\nu = 5/2$ fractional quantum Hall effect and reentrant integer quantum Hall effect.

1.8 Outline Of This Dissertation

The dissertation is divided into following chapters: Chapter 2 describes the experimental setups. In this chapter I will briefly introduce the principles of dilution refrigerator and the cooling procedures I routinely performed in the lab. The temperature measurements were performed using two different thermometry: a resistor thermometer and a quartz tuning fork viscometer. The electrical measurements setup will be mentioned in the end.

In chapter 3 I will present a study of the temperature dependence of the magnetoresistance of the reentrant integer quantum Hall effect in the second Landau level. We find a unique peak signature which can be used to define the onset temperature of the reentrant integer quantum Hall effect. From an analysis of the onset temperature, we find that the Coulomb energy is the relevent energy scale of the reentrant integer quantum Hall effect in the second Landau level. Such a finding indicates the

collective nature of the reentrant integer quantum Hall effect in the second Landau level.

In chapter 4 I will discuss the drastically different onset temperatures of the reentrant integer quantum Hall effect in the second and third Landau level. This finding is in quantitative disagreement with the Hartree-Fock theory of the bubble phases which is thought to describe these reentrant states. Our results indicate that the number of electrons per bubble in either the second or the third Landau level is likely different than predicted.

Chapter 5 continues the study of the reentrant integer quantum Hall effect in the fourth and the fifth Landau levels. I will report a strong Landau level dependence of the energy scales of reentrant integer quantum Hall effect. We find the cyclotron energy scale becomes important in these reentrant integer quantum Hall effects in high Landau levels. The Landau level dependence is possibly linked to the different microscopic structures of bubble phases predicted in different Landau levels.

In chapter 6 I will report a separate study on the impact of alloy disorder on the $\nu = 5/2$ fractional quantum Hall effect. Alloy disorder is controlled by the aluminum content x in the $Al_xGa_{1-x}As$ channel of a quantum well. We find that the $\nu = 5/2$ state is suppressed with alloy scattering. To our surprise, in samples with alloy disorder $\nu = 5/2$ state appears at significantly reduced mobilities when compared to samples in which alloy disorder is not the dominant scattering mechanism. Our results highlight the distinct roles of the different types of disorder present in these samples, such as the short-range alloy and the long-range Coulomb disorder.

2. EXPERIMENTAL SETUP

Low electron temperature is a pivotal experimental condition in studying the correlated ground states in a two dimensional electron gas. For example, early magnetotransport data has shown that the reentrant integer quantum Hall effect (RIQHE) develops at temperature lower than 50mK and has sensitive response to the temperature changes [25, 39]. In order to reliably measure their magnetotransport features and especially their temperature dependence, there are two major challenges: to cool the actual electron temperature below 10mK; and to create a stable temperature environment of the sample. We overcome the challenges by implementing a home-made ^{3}He immersion cell in a dilution refrigerator. In this chapter, I will review the basic principles of dilution refrigerator and the setup of ^{3}He immersion cell which we utilize to further improve the base temperature of the refrigerator. I will discuss several benefits of the ^{3}He immersion cell to our experiments. One important benefit is that the ^{3}He immersion cell enables a quartz tuning fork viscometry. Such a quartz viscometer can be used to accurately measure the temperature with a short relaxation time. The ^{3}He immersion cell can also create a stable temperature environment by advantage of the large thermal mass of liquid ^{3}He. The temperature stability is a critical experimental condition in studying the fine transport features of the RIQHE as well as their rapid temperature dependence.

Following the cooling of the samples, the magnetotransport data was obtained by electrical measurements with standard lock-in technique. It is important that low excitation is used in the measurements to avoid self-heating. I will describe our setup of the electronics which satisfies these experimental conditions.

2.1   The Dilution Refrigerator And Its Cooling Procedures

The ^{3}He/^{4}He dilution refrigerator has been an indispensable tool in studying low-temperature quantum phases because of its capability to provide continuous cooling in the milli-Kelvin regimes. The principle of dilution refrigerator was historically proposed by Heinz London with a simple physics core: below 0.87 K the ^{3}He/^{4}He mixture undergoes a phase separation into ^{3}He concentrated phase and ^{3}He dilute phase and the enthalpy of the ^{3}He in each phase is different [40]. Therefore, pumping on the dilute phase causes the ^{3}He to migrate from the concentrated phase into the dilute phase. ^{3}He absorbs energy in this process which leads to the cooling of the environment. The finite concentration of ^{3}He in the dilute phase at absolute zero temperature limit is the key to an effective cooling in the milli-Kelvin regimes. In contrast, pumping on the pure ^{4}He liquid can only cool the system down to about 1 Kelvin since the vapor pressure vanishes exponentially as temperature decreases to absolute zero.

Practically in our refrigerator, the cooling system consists of four stages specified in Fig 2.1. The first stage is called 1 K pot where temperature is usually kept at ~1.4 K by continuous pumping on the liquid ^{4}He. With 1 K pot running steadily, the mixture is condensed into the mixing chamber and filled up into the still. In order to reduce the mixture temperature to below the phase separation point, we start to pump on the still where the ^{3}He evaporates more preferentially due to its large vapor pressure compared to that of the ^{4}He. The still hence serves as the second cooling stage and is maintained at ~600 mK by an attached heater for better cooling power. As the phase separation continues, the cooling at the ^{3}He/^{4}He interface sets in which can bring the mixing chamber temperature down to a base temperature of ~5 mK. The mixing chamber is the third cooling state and also the coldest part in our refrigerator. To maintain the base temperature in the mixing chamber, the evaporated mixture has to be liquified and cooled again through the first two stages in their circulation path back into the mixing chamber.
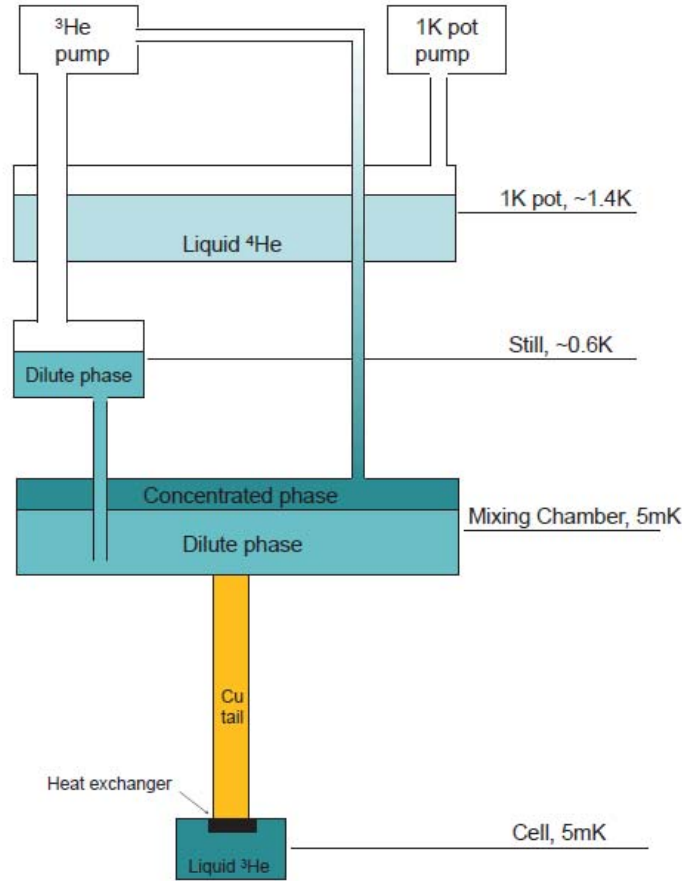
Figure 2.1. Schematic diagram of our custom-designed dilution refrigerator in Oxford Instruments. Dilute and concentrated phases of ^{3}He/^{4}He mixture are marked in the still and mixing chamber. The yellow part represents the copper tail. See references in the Operator's Handbook of Oxford Instruments [43]

2.2 The ^{3}He Immersion Cell

Although base temperature is already achieved in the mixing chamber, a direct attachment of sample to mixing chamber fails to cool the actual electronic temperature down to the base temperature. One of the main mechanisms responsible for this is the Kapitza boundary resistance between the sample and its thermal environment [40]. The Kapitza boundary resistance mainly results from acoustic mismatch

which leads to the scattering of the phonon at the interface of different materials. Since the Kapitza boundary resistance scales with T^{-3}, it becomes increasingly difficult for the thermal energy to dissipate out of the samples at ultra low temperature. One way to reduce this thermal resistance is to increase the contact area between the two different materials.
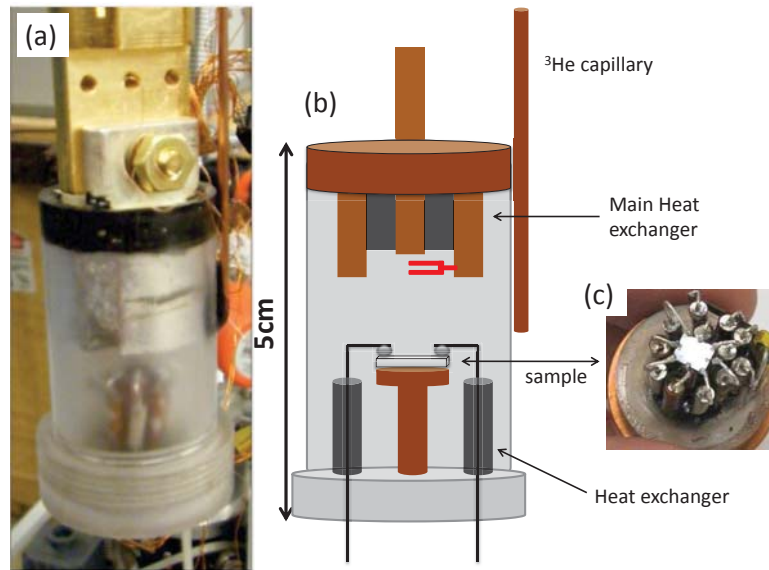
Figure 2.2. (a) The photo of ^{3}He immersion cell; (b) The schematics of the cell. The brown color represents copper, the black color represents silver and the translucent region represents the polycarbonate. The quartz tuning fork viscometer is colored red. The heat exchangers, sample and ^{3}He capillary are marked aside; (c) The photo of a GaAs/AlGaAs sample with eight heat exchangers soldered on corners. This picture is taken from Ref. [41]

To solve this problem in our setup, we installed the fourth home-made cooling stage, i.e. the ^{3}He immersion cell. As seen in the Fig 2.1, the cell is connected to the mixing chamber via a copper tail with a heat exchanger at its bottom [41]. The heat exchanger contains compressed silver powder which ensures a large surface area in contact with the outside. Fig 2.2 shows a more detailed schematics of the immersion cell along with the actual photo of it. In addition to the main heat exchanger, there are a dozen similar heat sinks to be soldered onto the indium contacts of the sample.

Finally, the cell can be filled with liquid ^{3}He condensed through a capillary which is in good thermal contacts with the first three cooling stages.

There are three benefits of implementing the ^{3}He immersion cell in our dilution refrigerator. First, as a good thermal conductor the liquid ^{3}He can take advantage of the large surface area of all the silver powdered heat exchangers which are immersed into it. Therefore the Kapitza boundary resistances between the sample and the cell as well as the cell and the copper tail can be effectively reduced. A good thermal equilibrium can be established between the sample and the mixing chamber through the copper tail to cool the sample electrons to the mixing chamber temperature. Therefore, the electron temperature in our sample can reach a record low value of $\sim$5 mK. Second, the ^{3}He liquid is viscous at ultra low temperature and its viscosity has a strong temperature dependence. By installing a quartz tuning fork in the ^{3}He immersion cell, we are able to measure the cell temperature or equivalently sample temperature from a calibrated temperature-viscosity curve [41]. Since the viscosity is magnetic field independent, the quartz tuning fork can accurately measure the temperature in a strong magnetic field in our magnetotransport experiments. Third, due to its large heat capacity, the ^{3}He liquid can serve as a thermal ballast which stabilizes the sample temperature. A stable temperature environment is a critical experimental condition in capturing the sharp features of the RIQHE and in studying their rapid temperature dependence.

2.3   Temperature Measurements

One of the main goals in our experiments is to measure the small energy gap of the fragile fractional quantum Hall effect such as the $\nu = 5/2$ fractional quantum Hall effect. The largest contribution in experimental error of the energy gap comes from temperature measurement since it is very difficult to determine the temperature in ultra-low temperature regimes. For example, the Kapitza boundary resistance can create a significant temperature difference between the thermometer and the environ-

ment. In another words, it may take a long relaxation time for the thermometer to reach equilibrium with the environment.

In our experiments we use two thermometers in temperature measurements: one is the quartz tuning fork viscometer [41] and the other one is a calibrated Speer carbon composition resistor [42]. The quartz viscometer is immersed in the ^{3}He cell and the Speer thermometer is installed onto the mixing chamber stage. As described above, when the system is in equilibrium and the magnetic field is zero, both the quartz viscometer and Speer thermometer should measure the same temperature. However, when we are scanning temperature, the readouts of both thermometers can be quite different. This is because the ^{3}He immersion cell has a large thermal mass and its temperature changes much slower than the mixing chamber. Nonetheless, since the quartz thermometer is located near the sample, it can measure the sample temperature in real time. Consequently, we trust the readout of the quartz thermometer in temperature scan experiments.

For magnetotransport measurements which are done at a constant temperature, we use both thermometers but in different temperature regimes. Below 100 mK, we choose the quartz viscometer by virtue of the strong temperature dependent viscosity of the liquid ^{3}He as well as zero magnetic field dependence. In contrast, the Speer thermometer has weak magnetic field dependence and corresponding error may become significant in such a low temperature regime. Close to 100 mK, however, the viscosity of liquid ^{3}He tends to be less sensitive with respect to temperature change although we can still use the quartz viscometer through a nonlinear calibration. Above 200 mK, the viscosity of liquid ^{3}He stays nearly independent of temperature. Instead, we turn to the Speer thermometer for more accurate temperature measurements. It is noted that the relative error of the Speer thermometer is very small in this temperature regime. Fortunately, most many-body states such as RIQHE and $\nu = 5/2$ fractional quantum Hall effect studied in this dissertation develop below 200 mK and the quartz viscometer alone can satisfy all our needs for temperature measurements.

While there are many methods to measure the viscosity of the liquid ^{3}He, the usage of quartz viscometer ensures a very fast measurement. The ideal model of the quartz viscometer can be treated as a LRC circuit [41]. As related to the dissipation component or namely resistor of this circuit, viscosity is found to be inversely proportionate to the square root of the quality factor. Moreover, the quality factor is linearly proportionate to the current specifically at resonance frequency. Therefore, a relation between the resonance current of the quartz viscometer and the viscosity of the liquid ^{3}He can be established. By further converting the viscosity into temperature, we are able to relate the resonance current directly to the temperature. In reality, we find that the calibration curve of resonance current versus temperature for a 20KHz quartz is almost linear under 100 mK.

The calibration of the quartz viscometer is very essential in each measurement. During the calibration, we drive the quartz viscometer by an AC voltage generator [41]. Ideally, the in-phase component of the current of a RLC circuit should have a frequency response function of a perfect symmetric Lorentzian shape. At resonance, the in-phase current component reaches maximum while concomitantly the out-of-phase current component becomes zero. However, the actual model of the quartz involves a small capacitor in parallel with the LRC circuit which leads to an asymmetry of the in-phase frequency response function. The resonance current in this non-ideal model has no simple relation to the viscosity which can introduce systematic error on temperature measurements. To correct this asymmetry, we add a cancellation capacitor by using a transformer [41]. We tune the cancellation capacitor to zero the out-of-phase current component at resonant frequency. This tuning process is done once in zero magnetic field before the temperature calibration of the resonance current of the quartz.

A practical issue of the quartz viscometer is that the new resonance frequency needs to be located whenever the temperature changes. The frequency scanning method can locate the resonant frequency but in a very time consuming way. Instead we turn to a self-lock circuit in measuring the quartz viscometer after tuning

the cancellation capacitor [41]. This self-lock technique can instantly measure the in-phase current at the resonant frequency by always locking the quartz viscometer to its resonance point. In this self-lock mode, we then calibrate the quartz viscometer by the Speer thermometer at several different temperature. We note that calibration coefficients have been very reproducible for the same quartz tuning fork during different cooldowns.

2.4 Electric Setup For Resistance Measurements

The electrical measurements are performed after cooling down the sample in our refrigerator. The most important elements in our electronic setup are lock-in amplifiers. The lock-in amplifier is a very powerful electronic device in recovering a small signal from a noisy environment. By using a reference signal of sinusoidal function, the lock-in amplifier can measure the input signal in a very narrow frequency domain at the reference signal frequency. Since the noise usually has a broad band width, the lock-in amplifier is able to reject most of the noise to obtain the low-noise level signal. Two lock-in amplifiers are used to measure the Hall voltage signal and longitudinal voltage signal respectively while another lock-in amplifier is used to measure the quartz tuning fork viscometer. In order to avoid self-heating effect in ultra-low temperature, the sample is biased with a very low excitation current of 2nA. Since the longitudinal voltage signal is normally very small, we further amplify it with a low-noise preamplifier of gain 100 before the signal being input into the lock-in amplifier.

We also note that a large noise can also come from the ground loop of our electronics. The ground loop refers to a noisy potential difference between different grounds. In our experiment, a ground loop can exist between the sample and the lock-in amplifier which adds a corresponding noise signal to the sample excitation. To break the ground loop, we use a transformer of gain 1 to pass only the AC excitation signal from the source module.

The sample we measured in the refrigerator is a 4mm×4mm square with eight indium-tin contacts on the four corners and the middle points of the four edges (shown in Fig 2.2). To make the Ohmic indium-tin contacts, indium-tin is firstly deposited onto the surface of the sample and then annealed in a forming gas atmosphere at 400 Celsius degrees for 10 minutes. Such a symmetric geometry of the contacts allows us to measure the Hall resistance and longitudinal resistance in different configurations. In reality, some of the contact configurations can produce a "bad" trace of the magnetoresistance. For example, it is found that in measuring the longitudinal voltage, one of the two sides can have a magnetic field dependent offset [44]. We test different contact configurations to find an optimal one which exhibits the best features of the magnetoresistance.

Finally, it is very convenient to measure the electron mobility of the sample in this square geometry. In zero magnetic field, we use the Van der Pauw methods to measure the electron mobility. This measurement can be done with the four corner contacts. We drive a larger excitation current of about 1μA through one edge and measure the voltage over the opposite edge. By rotating this configuration, we can obtain four resistivity R_1, R_2, R_3, R_4 successively. When these four resistivity are of close values, the sheet resistivity R_S of the 2DEG can then be calculated from the equation below:

$$R_S = \frac{\pi}{ln2} \times R_A; R_A = (R_1 + R_2 + R_3 + R_4)/4 \qquad (2.1)$$

The electron mobility can be calculated using equation $\mu = \frac{1}{neR_S}$. Here n is the areal density of the 2DEG and e is the electron charge.

2.5   Conclusions

To sum up, in this chapter I describe the dilution refrigerator and the ^{3}He immersion cell installed in it. ^{3}He immersion cell helps to cool the electron temperature to as low as 5mK and to create a stable temperature environment. These experimental conditions are critical in the study of the reentrant integer quantum Hall effects. I

also describe our temperature measurements with both a quartz tuning fork viscometer and the Speer resistor thermometer. The quartz tuning fork viscometer enables magnetic field independent temperature measurements. In the end, I describe the low excitation, low noise electronic setup in measuring the magnetoresistance of the sample.

3. THE COLLECTIVE NATURE OF REENTRANT INTEGER QUANTUM HALL STATES IN THE SECOND LANDAU LEVEL
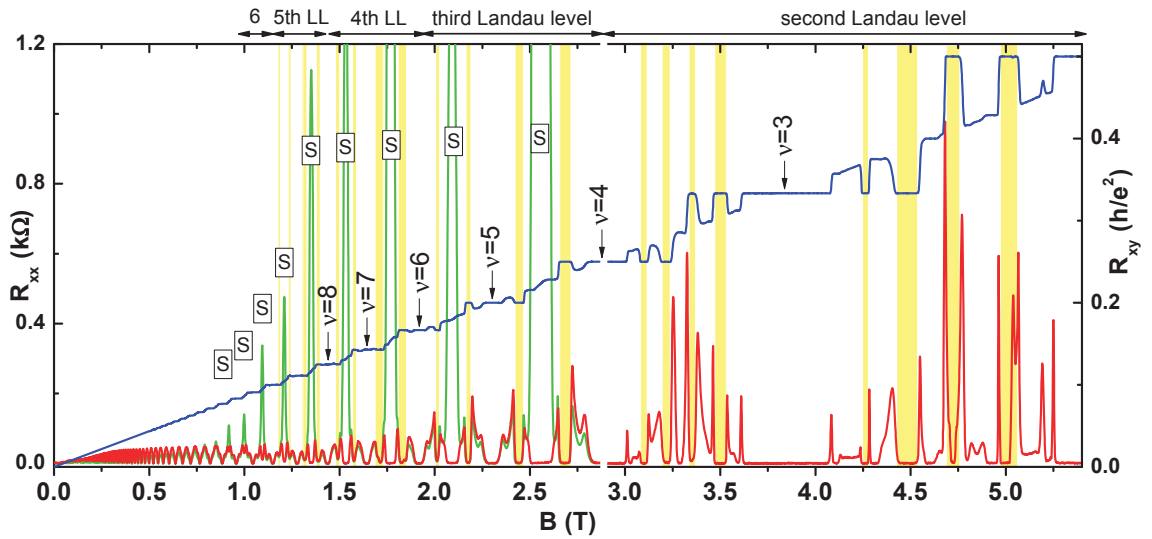
Figure 3.1. The Hall and longitudinal resistance measured from zero magnetic field up to the second Landau level. The second Landau level is measured at 6.9mK while the data at higher magnetic fields is measured at 77mK. The lowest six Landau levels are labeled on top axis with number 6 representing the sixth Landau level. The integer quantum Hall states are marked at corresponding integer filling factors. The reentrant integer quantum Hall states are shaded by yellow stripes and the stripe phases are marked by symbol S. The red trace and the green trace are measured in mutually perpendicular directions along crystalline axes [110] and [1$\bar{1}$0]. This data is measured in a high quality sample of mobility $15 \times 10^6 \text{cm}^2/\text{Vs}$ grown by M.J. Manfra group at Purdue. Part of the data is published in Ref. [114]

There is an astonishingly large number of ground states discovered in the two dimensional electron gas subjected to a magnetic field. In Fig 3.1, examples of rich ground states in this system are shown in our best magnetotransport trace measured in a high quality sample grown at Purdue. Among such a wide region of magnetic field from 0 Tesla to nearly 6 Tesla, the second Landau level is so far the most interesting region where correlated ground states of possible exotic nature keep emerging. Following the first observation of exotic even-denominator fractional quantum Hall state (FQHS), several other FQHSs at $\nu = 2 + 1/3, \nu = 2 + 2/3, \nu = 2 + 1/5, \nu = 2 + 4/5$ and $\nu = 2 + 2/5$ were also found to be fully quantized [35, 45]. Most recently, the ultra-low temperature achieved in our lab has led to a discovery of exotic FQHS at $\nu = 2 + 6/13$ [36]. The eight reentrant integer quantum Hall states (RIQHSs) form another set of prominent ground states in the SLL. They were historically discovered by J.P. Eisenstein et al. at temperature below 50 mK and in a sample of electron mobility over $3 \times 10^7 \text{cm}^2/\text{Vs}$ [25]. Although their transport signatures are consistent with electron localization in the topmost energy level [25], the nature of the localization is not yet well understood. Depending on the relative importance of the electron-electron interactions, the ground state can be either an Anderson insulator or a collectively pinned electron solid.

FQHSs owe their existence to the presence of the inter-electronic Coulomb interactions [4, 5]. Since FQHSs and RIQHSs alternate in the SLL, it was argued that Coulomb interactions must be important and, therefore, the RIQHSs in the SLL must be electron solids [25]. Subsequent density matrix renormalization group [46] and Hartree-Fock calculations [29] also favored the electron solid picture and predicted the solid phase similar to the Wigner crystal, but having one or more electrons in the nodes of the crystal. Recently reported weak microwave resonances in one such RIQHS are suggestive of but are far from being conclusive on the formation of a collective insulator [33]. Our understanding of the RIQHSs in the SLL, therefore, is still in its infancy and the collective nature of these states has not yet been firmly established.

To understand the nature of RIQHSs, we conduct magnetotransport measurements with varying temperatures. We discover a feature in the temperature dependent magnetoresistance which so far has only been observed in the RIQHSs in the SLL and which we use to define the onset temperature of these states. The scaling of onset temperatures with the Coulomb energy reveals that Coulomb interactions play a central role in the formation of RIQHSs and, therefore, these reentrant states are exotic electronic solids rather than Anderson insulators. We also find an unexpected trend of the onset temperatures within each spin branch. This trend is inconsistent with current theories and can be understood as a result of a broken electron-hole symmetry. Explaining such a broken symmetry of the RIQHSs is expected to impact our understanding of a similar asymmetry of the exotic FQHSs of the SLL, including the one at $\nu = 5/2$.

3.1 Magnetotransport Signatures Of Reentrant Integer Quantum Hall States In The Second Landau Level

We performed magnetotransport measurements on a high quality GaAs/AlGaAs sample of density $n = 3.0 \times 10^{11} cm^{-2}$ and of mobility $\mu = 3.2 \times 10^7 cm^2/Vs$. The sample is immersed into a ^{3}He cell equipped with a quartz tuning fork viscometer used for B-field independent thermometry.

In Fig 3.2 we show the dependence of the Hall resistance R_{xy} and longitudinal resistance R_{xx} in the SLL on the magnetic field B (bottom scale) and on the Landau level filling factor ν (top scale). Because of the lifted spin degeneracy, the lower of the two energy levels of the SLL is occupied for $2 < \nu < 3$ hence the term lower spin branch. $3 < \nu < 4$ corresponds to the occupation of the upper spin branch. Shown in Fig 3.2 there are several regions of ν for which R_{xy} has plateaus quantized to an integer, i.e. $R_{xy} = h/ie^2$ with $i = 2, 3$, and 4. Of these plateaus the ones stretching at $\nu < 2.17$, $2.83 < \nu < 3.17$, and $\nu > 3.83$ are quantized to $h/2e^2$, $h/3e^2$, and $h/4e^2$ and contain the filling factors $\nu = 2, 3$, and 4, respectively. These regions are to the well
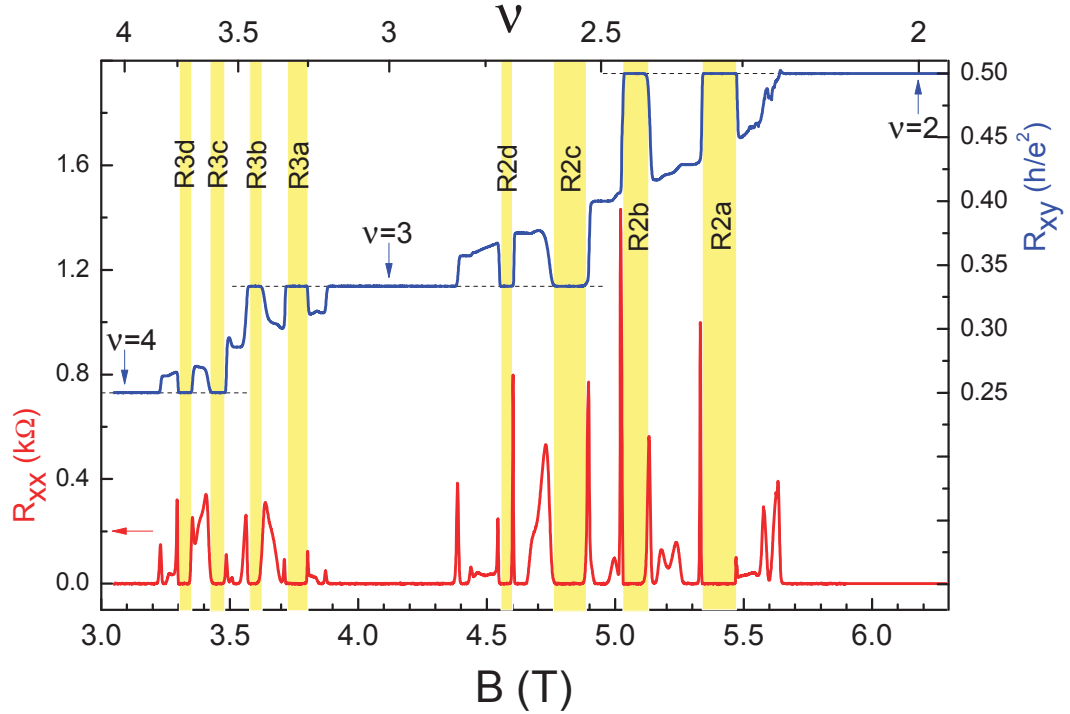
Figure 3.2. The Hall and longitudinal resistance of the eight RIQHSs in the SLL at 6.9 mK. The data of Hall resistance is published in Ref. [113] and the data of longitudinal resistance is published in Ref. [117]

known integer quantum Hall plateaus. In contrast, other eight plateaus of Fig 3.2 are quantized to an integer but are not centered around an integer ν. For example the shaded region of Fig 3.2 labeled $R2a$ exhibits $R_{xy} = h/2e^2$ and it stretches between $2.26 < \nu < 2.32$, a region which does not contain $\nu = 2$. These eight states are the RIQHSs [25] and we label the ones located between $2 < \nu < 3$ with $R2a$, $R2b$, $R2c$, and $R2d$ and the ones betwee $3 < \nu < 4$ with $R3a$, $R3b$, $R3c$, and $R3d$. RIQHSs have historically been predicted [22] and observed [23, 24] in high Landau levels (i.e., $\nu > 4$), but in contrast to the SLL, in high Landau levels there are only four RIQHSs in each Landau level.
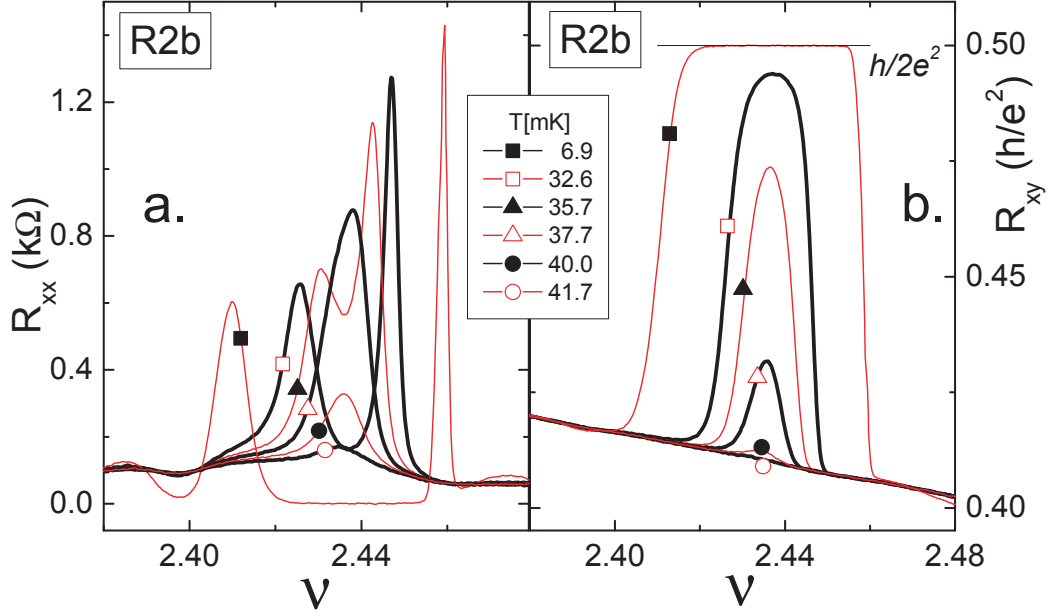
Figure 3.3. The temperature evolution of the RIQHS labeled *R2b*. This data is published in Ref. [113]

Because of the delicate nature of the RIQHS in the SLL [25, 36, 39, 45, 47–54] there is only scarce information available on their temperature dependence [39, 50, 53]. In Fig 3.3(a) and 3.3(b) we show the detailed temperature evolution of the longitudinal resistance R_{xx} and R_{xy} of *R2b*, respectively. The $R_{xx}(B)|_{T=6.9mK}$ curve has a wide zero flanked by two sharp spikes. As the temperature is raised, the spikes in R_{xx} persist but they move closer to each other and the width of the zero decreases. At 32.6 mK $R_{xx}(B)$ does still exhibit the two spikes but instead of a zero it has a nonzero local minimum. The location in B field of this minimum is T independent and it defines the center $\nu_c = 2.438$ of the *R2b* state. At 35.7 mK the two spikes of $R_{xx}(B)$ have moved closer to each other and between them there is still a local minimum, albeit with a large resistance. A small increase in T of only 2 mK leads to a qualitative change. Indeed, in contrast to curves at lower T, $R_{xx}(B)|_{T=37.7mK}$ exhibits a single peak only. As the temperature is further raised, this single peak rapidly decreases

until it merges into a low resistance background. Simultaneously with the described changes of R_{xx}, R_{xy} evolves from the quantized value $h = 2e^2$ to its classical value $B/ne = h/\nu_c e^2$.

3.2 Onset Temperatures And Stability Diagram Of Reentrant Integer Quantum Hall States

The behavior seen in Fig 3.3 can be better understood by measuring T dependence at a fixed ν. In Fig 3.4 we show R_{xy} versus T near the center ν_c of the various RQIHSs. It is found that R_{xy} assumes the classical Hall resistance at high T and it is quantized to $h = 2e^2$ or $h = 3e^2$ at low T. Since 80% of the change in R_{xy} between these two values occurs over only 5 mK, this change is very abrupt and it clearly separates the RIQHS at low T from the classical gas at high T. We interpret the inflection point in R_{xy} versus T as being the onset temperature T_c of the RIQHS. For reliable measurements in the vicinity of T_c the temperature is swept slower than 10 mK/h.

A transition from the classical Hall value to a quantized Rxy with decreasing T is observed not only for the RIQHSs in the SLL but also in the vicinity of any developed integer or fractional quantum Hall state and it is due to localization in the presence of a B field. As seen in Fig. 4, the $R_{xx}(T)|_{\nu=fixed}$ curves for the RIQHSs are nonzero at high T, they vanish at low T, and they exhibit a sharp peak at the onset temperature T_c defined above. In contrast, $R_{xx}(T)|_{\nu=fixed}$ of a quantum Hall state changes monotonically without the presence of a peak. We found no reports in the literature of a similar peak in any other ground state of the 2DEG. The sharp peak in $R_{xx}(T)|_{\nu=fixed}$ is, therefore, a signature of localization so far only observed in the RIQHSs of the SLL and the peak temperature can be used as an alternative definition for the onset temperature T_c.

Fig 3.5 represents the stability diagram of the RIQHSs in the $\nu^* - T$ plane. Here $\nu^* = \nu - 2(3)$ is the partial fill factor of the lower (upper) spin level. As described earlier, at a given ν the RIQHSs develop below the temperature of the peak in the
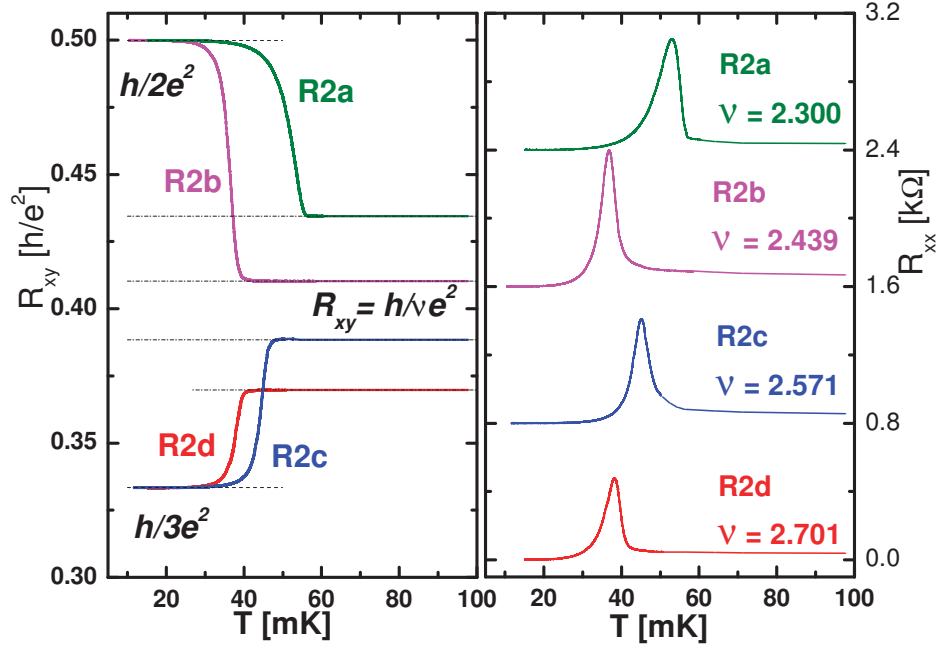
Figure 3.4. The evolution of the magnetoresistance of RIQHSs of the lower spin branch with temperature near the center ν_c of each RIQHS. For clarity, $R_{xx}(T)$ curves are shifted vertically by 0.8 $k\Omega$. This data is published in Ref. [113]

$R_{xx}(T)|_{\nu^*=fixed}$ curve. Such peaks are shown in Fig 3.4 for $\nu^* \approx \nu_c^*$, but similar peaks are also present for nearby filling factors (not shown). Open symbols in Fig. 5 are the temperatures of the peak as plotted against ν^*. Similarly, the RIQHSs develop between the spikes of the $R_{xx}(\nu)|_{T=fixed}$ curves, such as the ones shown in Fig 3.3(a) The filling factors ν^* of the spikes for each RIQHS measured at a given temperature are marked with closed symbols in Fig 3.5. The excellent overlap of the two data sets in Fig 3.5 shows that the two definitions used above selfconsistently define the stability boundary of each RIQHS. The shaded areas within each boundary of Fig 3.5 represent the RIQHSs. FQHSs can develop only outside these shaded areas. The locations ν_{high}^* and ν_{low}^* of the spikes of the $R_{xx}(\nu)|_{T=fixed}$ curve measured at the lowest $T = 6.9$ mK of our experiment are listed in Table 3.1.
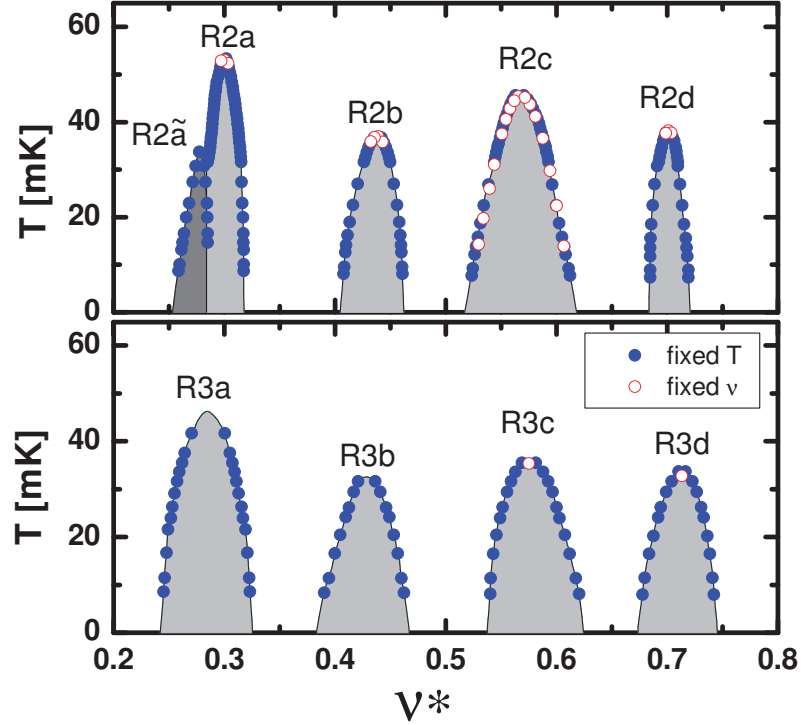
Figure 3.5. The phase boundaries of the eight RIQHS in the SLL in the $\nu^* - T$ plane. The RIQHSs are stable within the shaded areas. Below 33 mK the $R2a$ state has a splitoff state labeled $R2\tilde{a}$. This data is published in Ref. [113]

We note that the $R2a$ state is different from the rest of the RIQHSs as it splits into two RIQHSs with a decreasing temperature. Such a split is signaled by an R_{xy} deviating from $h = 2e^2$ as well as a nonzero R_{xx} in the vicinity of $\nu = 2 + 2/7$ and it has already been reported in Ref. [45]. The split-off RIQHS is marked as $R2\tilde{a}$ and with a darker shade in Fig 3.5. We note that our data are similar to that in Ref. [25] in that the Ria, $i = 2, 3$ is the most stable state. Other studies find the $R2c$ state to be the most stable of RIQHSs [33, 39, 47–54].

3.3 Particle-Hole Asymmetry

Each stability boundary shown in Fig 3.5 can be fitted close to their maxima with a parabolic form $T_c(\nu^*) = T_c(\nu_c^*) - \beta(\nu^* - \nu_c^*)^2$. The obtained parameters are listed in Table 3.1. T_c obtained from the fit is within 1 mK from the peak temperature obtained from Fig 3.4. The centers ν_c^* of the RIQHSs in the upper spin branch are in excellent agreement with the earlier reported values [25]. Those of the upper spin branch, however, have not yet been documented and they differ significantly from those of the lower spin branch. Indeed, $\nu_{R2\alpha}^* \neq \nu_{R3\alpha}^*$ for $\alpha = a, b, c$, or d, the difference being the largest for the states a and d. Such a difference is not expected from the theory [29,46] and we think it is due to the interaction of the electrons in the topmost Landau level with those in the filled lower levels. Furthermore, we establish that the centers ν_c^* of RIQHSs in both spin branches obey particle-hole symmetry, as assumed by the theory [29, 46]. In short $\nu_{c,Ria}^* = 1 - \nu_{c,Rid}^*$, $\nu_{c,Rib}^* = 1 - \nu_{c,Ric}^*$ for $i = 2, 3$, relations which hold within our measurement error for the filling factor of ± 0.003.

In contrast to the centers of RIQHSs, other parameters of RIQHSs from Table 3.1 do not obey particle-hole symmetry. These parameters are the maximum onset temperatures $T_c(\nu_c^*)$, the fit parameter β describing the curvature of the stability diagrams near $T_c(\nu_c^*)$, and the widths $\Delta\nu = \nu_{high}^* - \nu_{low}^*$ of the stability regions of the

Table 3.1

Parameters extracted from the ν^*-T diagram. T_c and β are in units of mK.

	R2a	R2b	R2c	R2d	R3a	R3b	R3c	R3d
ν_c^*	0.300	0.438	0.568	0.701	0.284	0.429	0.576	0.712
$T_c(\nu_c^*)$	53.0	37.1	45.8	38.0	46.3	32.3	36.1	33.8
$\beta \times 10^{-4}$	10	3.9	2.4	8.5	2.1	2.0	1.6	2.3
ν_{high}^*	0.317	0.461	0.613	0.719	0.324	0.463	0.621	0.742
ν_{low}^*	0.258	0.407	0.523	0.684	0.245	0.388	0.540	0.677

RIQHSs at $T = 6.9$ mK Indeed, particle-hole symmetry within a spin branch would imply a scaling of T_c with the Coulomb energy E_C and, therefore, a monotonically decreasing $T_c(\nu_c^*)$ with an increasing ν_c^*. Here $E_C = e^2/\epsilon l_B$ and $l_B = \sqrt{\hbar/eB}$ is the magnetic length. Data from Table 3.1, however, clearly show that contrary to this expectation $T_c(\nu_c^* = 0.568) > T_c(\nu_c^* = 0.438)$ [39]. We thus find that the particle-hole symmetry within one spin branch assumed in current theories [29,46] is violated. The nonmonotonic dependence of T_c on ν_c^* is, furthermore, at odds with the sequence of the one- and two-electron bubbles suggested [29,46]. These findings are puzzling and they show that there is still much left to be understood about the RIQHSs. Possible causes include Landau level mixing, disorder, or finite thickness effects. The origin of the broken symmetry described above is most likely related to and, therefore, it will influence the understanding of a similar symmetry breaking of the Pfaffian and anti-Pfaffian construction for the $\nu = 5/2$ FQHS [55–62].

3.4 Scaling Of Coulomb Energy Between Two Spin Branches

The onset temperatures $T_c(\nu_c^*)$ in the higher spin branch are consistently smaller than those in the lower spin branch. We notice, however, a startlingly similar dependence within each spin branch. A particularly revealing plot is that of the reduced onset temperatures $T_c(\nu_c^*)/E_C$ against the filling factor ν_c^*. As shown in Fig 3.6, there is a surprisingly good collapse of $T_c(\nu_c^*)/E_C$ for the different spin branches. This collapse shows that Coulomb interactions play a central role in the formation of the RIQHSs in the SLL and provides direct evidence that these states reflect collective behavior of the electrons rather than single particle localization. The lack of collapse of $T_c(\nu_c^*)/\hbar\omega_C$ (not shown) means that $T_c(\nu_c^*)$ does not scale with the cyclotron energy $\hbar\omega_C$.

In a recent study an activated dependence of $R_{xx}(T)$ is found for the $R2c$ state [53]. In our sample we find a significant deviation from such a dependence and, as a consequence, the definition of an activation energy is no longer possible. Fig 3.7
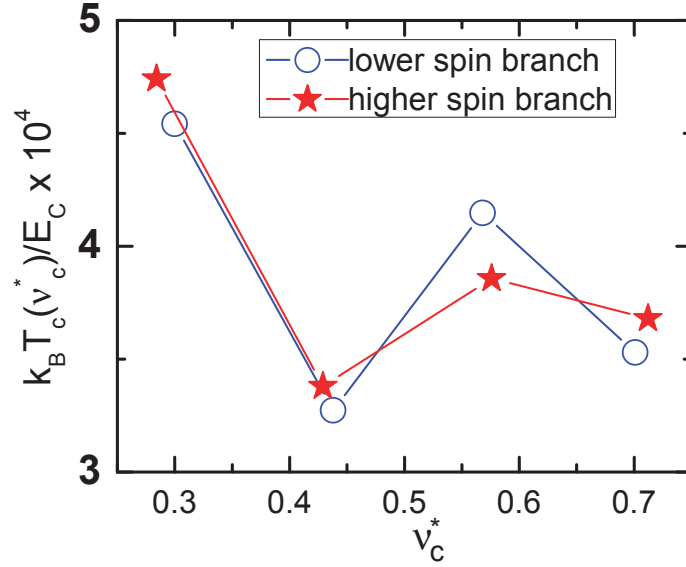
Figure 3.6. The variation with the filling factor ν_c^* of the reduced onset temperatures $T_c(\nu_c^*)/E_C$ at the center of the RIQHSs in the SLL. Lines are guides to the eye. This data is published in Ref. [113]

shows such a plot for the $R2c$ state, together with the activated resistance of a suitably chosen FQHS measured in order to rule out thermometry artifacts. Our data suggest that nonactivated behavior might be an inherent property of the RIQHSs. The peak in the $R_{xx}(T)|_{\nu=fixed}$ curves could be due to interpenetrating RIQHS, a collective low T insulator and the high T classical electron fluid. In such an interpretation the nonactivated behavior seen in Fig 3.7 is a consequence of the coexistence of these two phases.

3.5 Conclusions

In this chapter I report an unexpected sharp peak in the temperature dependence of the magnetoresistance of the RIQHS in the second Landau level. This peak defines the onset temperature of these states. We find that in different spin branches the onset temperatures of the reentrant states scale with the Coulomb energy. This
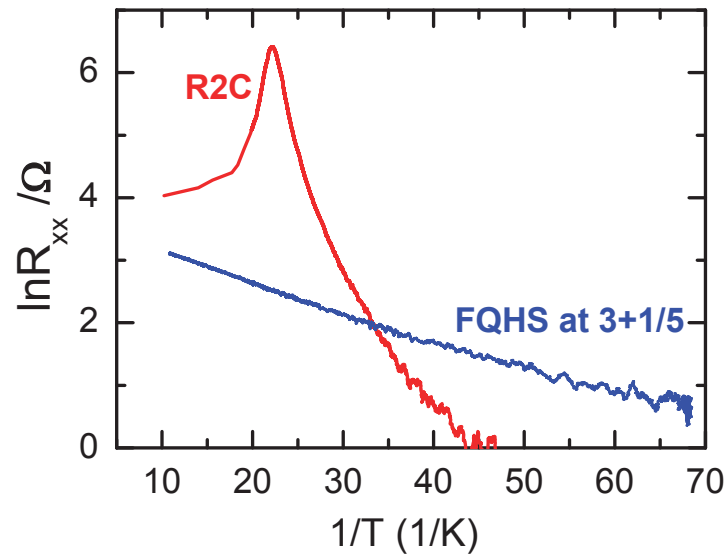
Figure 3.7. Arrhenius plot for $R2c$ and for the $\nu = 3+1/5$. This data is published in Ref. [113]

scaling provides direct evidence that Coulomb interactions play an important role in the formation of these reentrant states evincing their collective nature

4. CONTRASTING ENERGY SCALES OF THE REENTRANT INTEGER QUANTUM HALL STATES

We continue similar investigation of reentrant integer quantum Hall states (RIQHSs) in the third Landau level (TLL). In contrast to RIQHSs in the SLL, the RIQHSs in the TLL develop in much higher temperature regimes (> 100 mK) and in a Landau level where no FQHSs exist [23, 24]. The number of RIQHSs also differs between the two Landau levels since only four RIQHSs form in the TLL whereas eight RIQHSs form in the SLL [25]. However, despite of these differences, their dc and microwave transport data share similar features [23–25, 31, 33].

The theoretically predicted origins of RIQHSs in both Landau levels are associated with the bubble phases but of different electronic structures, i.e. number of electrons per bubble. In the second Landau level (SLL) both two and one electron bubble phases are predicted to form [29] while in the third Landau level (TLL) only two electron bubble phases are expected [27–29,63,65]. These theories, however, have their limitations. The Hartree-Fock approach, the only one used for bubble phases both the TLL [29,63] and the SLL [29], is exact only in the limit of large LL occupation [64,66], and may therefore not capture all aspects of bubbles at the lowest LL occupation, i.e. those in the second and third LLs. In addition, the presence of competing nearby fractional quantum Hall states in the SLL [36,45] is likely to enhance fluctuations and may therefore influence electron ordering. Finally, none of the theoretical techniques include LL mixing, an electron-electron interaction effect known to strongly affect the energy gaps of fractional quantum Hall ground states in the SLL [55,56,59,61,62,69, 70].

In this chapter, we will report sharp peaks in the temperature dependent longitudinal resistance of the RIQHSs in the TLL which are similar to those of the RIQHSs in

the SLL, highlighting their common origin. These sharp peaks allowed us to extract the onset temperatures of the RIQHSs in the TLL which enabled a quantitative comparison of the RIQHSs forming in the TLL with those in the SLL as well as with the theoretically predicted bubble phases. Our measurements of the onset temperatures are at odds with the cohesive energy calculations obtained within the Hartree-Fock approximation and indicate that the assignment of the RIQHSs to the various bubble phases is likely different than predicted.

4.1 Magnetoresistance Of Reentrant Integer Quantum Hall States In The Third Landau Level
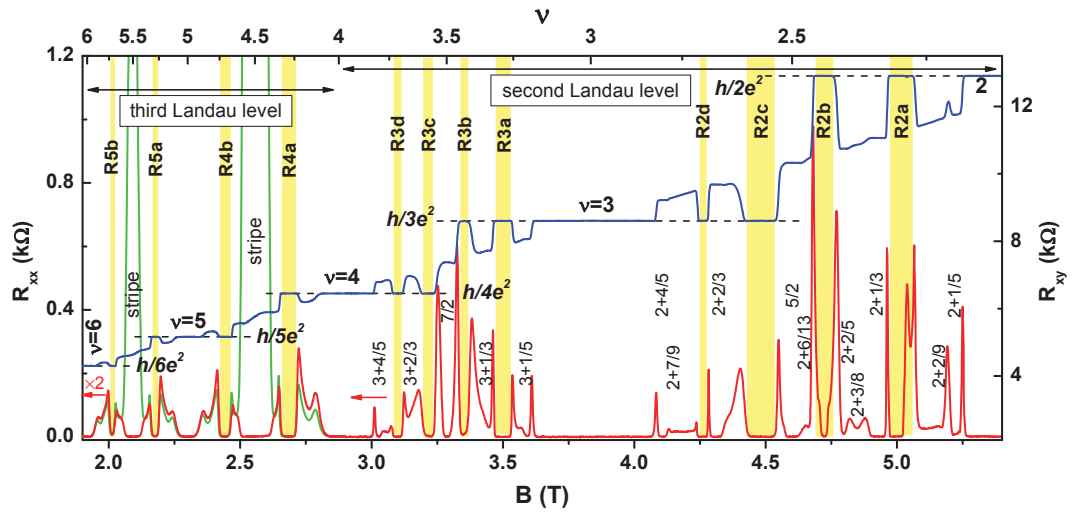
Figure 4.1. The magnetoresistance in the second ($2 < \nu < 4$) and third ($4 < \nu < 6$) Landau levels as measured at 6.9 mK and 77mK, respectively. RIQHSs are marked by shaded stripes and FQHSs by their filling factors. In the TLL the two R_{xx} traces shown are measured along mutually perpendicular directions and, for clarity, are magnified by a factor two. This sample is grown by J. Watson and M.J. Manfra at Purdue. This data is published in Ref. [114]

We measured a high quality 2DEG confined to a 30 nm wide GaAs/AlGaAs quantum well with a density $n = 2.8 \times 10^{11} \text{cm}^{-2}$ and mobility $15 \times 10^6 \text{cm}^2/\text{Vs}$ grown at Purdue.

In Fig 4.1 we show the longitudinal magnetoresistance R_{xx} and the Hall resistance R_{xy} plotted against B and filling factor ν in the SLL and TLL. Here $\nu = nh/eB$, where h is Planck's constant and e is the elementary charge. It is important to appreciate that a completely filled orbital Landau level is spin-split into two distinct energy levels and, hence, its filling factor is $\nu = 2$. Therefore the lowest Landau level corresponds to filling factors $\nu < 2$, the SLL corresponds to $2 < \nu < 4$, while the TLL to $4 < \nu < 6$.

The well known integer quantum Hall states are seen in Fig 4.1 as plateaus in R_{xy} quantized to h/ie^2, with $i = 2, 3, 4, 5$, and 6. Each of these plateaus straddle the corresponding integer filling factor $\nu = i$. As B is varied, R_{xy} deviates from these plateaus. There are, however, other regions for which R_{xy} returns to an integer quantization but, in contrast to the plateaus of the integer quantum Hall states, these plateaus develop at ranges of ν which do not contain any integer values. These features define the RIQHSs [23–25, 30]. As an example, the RIQHS labeled $R2c$ in Fig 4.1 has $R_{xy} = h/3e^2$ and it stretches between $2.54 < \nu < 2.60$, a region which does not contain any integers. Quantization of R_{xy} is accompanied by a vanishing R_{xx}. Altogether, in the SLL there are eight RIQHS labeled $R2a$, $R2b$, $R2c$, $R2d$, $R3a$, $R3b$, $R3c$, and $R3d$ [25], while in the TLL there are only four such states labeled $R4a$, $R4d$, $R5a$, and $R5d$ [23, 24]. The RIQHSs are clearly marked and shaded in Fig 4.1.

In Fig 4.1 we also identify anisotropic ground states called stripe phases [22, 66] in the vicinity of $\nu = 9/2$ and $11/2$ [23, 24], a very strong fractional quantum Hall state (FQHS) at $\nu = 5/2$ [8] with a gap of 0.50 K, a well quantized $\nu = 2 + 2/5$ FQHS, and we discern developing FQHSs at $\nu = 2 + 6/13, 2 + 2/9, 2 + 7/9$, and $2 + 3/8$ [36, 45]. We also observe a split-off RIQHS at B-fields exceeding that of the $R2a$ state which was discovered in Ref. [45] and studied in detail in previous chapters. In addition to

these known aspects, we observe a new feature in the Hall resistance at $B = 5.196$ T or $\nu = 2.214$. This feature is a clear deviation from the classical Hall line and it may signal the development of another RIQHS.

4.2 Common Transport Signatures In The First Two Excited Landau Levels
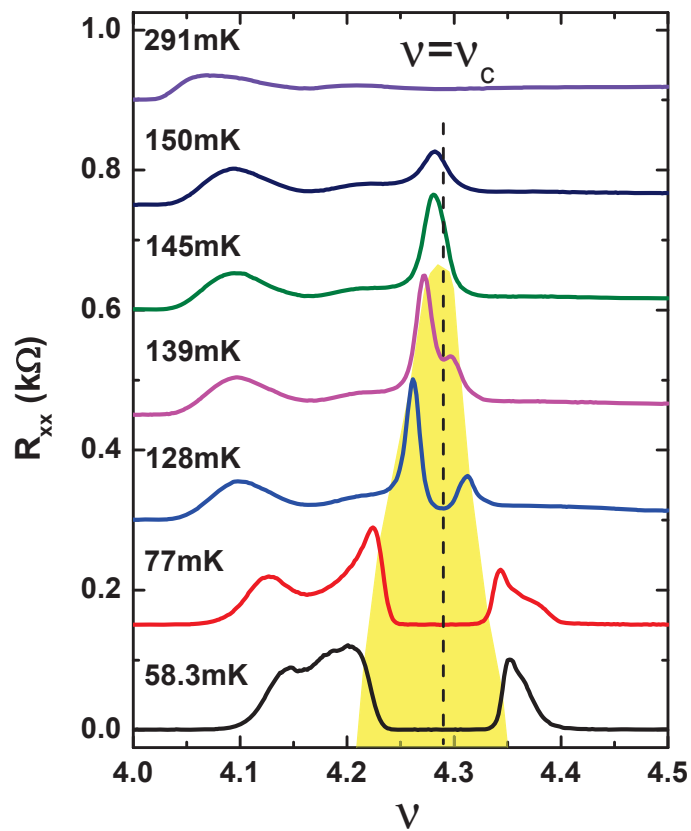
Figure 4.2. The evolution with temperature of the $R4a$ RIQHS of the third Landau level. For clarity traces are shifted by 150Ω relative to another and the reentrant region is shaded. This data is published in Ref. [114]

In the following we establish two common transport signatures of the RIQHSs in the SLL and TLL: spikes flanking the vanishing regions of the R_{xx} versus B curves and a peak in the temperature dependent R_{xx}. These findings further strengthen the argument that the RIQHSs of different LL have similar origins.

One similarity between the RIQHSs in the SLL and TLL we find is the presence of two sharp spikes in the flanks of the vanishing region of the R_{xx} versus B curves, i.e. the edges of the shaded areas of Fig 4.1. Such spikes are known to be present in the flanks of the RIQHSs in the SLL [36,45] and now we observe them in the TLL as well. With the exception of the data in Ref. [71], earlier R_{xx} versus B curves showed a single broad peak in the region separating the RIQHS from the nearby integer plateaus; the width at half height of this peak for RIQHSs near $\nu = 9/2$ was measured to be about 0.05 T. In contrast, our data in Fig.1 at the corresponding fields, i.e. in the range of $2.7 \div 2.85$ T, has a more complex structure which exhibits a sharp spike at 2.72 T of width 0.016 T. We think that the richer structure in R_{xx} and the presence of the sharp spikes are due to an improved sample uniformity.

Contrary to a previous report [72], in our sample there are no magnetoresistance features which may be associated with a FQHS in the TLL. We find that the $\nu = 4 + 1/5$ and $4 + 4/5$ filling factors, as seen in Fig 4.1 and in Fig 4.2, are part of the complex behavior of R_{xx} described above. Local minima do develop, but they are not located at $\nu = 4 + 1/5$ or $4 + 4/5$ and, furthermore, they are not accompanied by a quantized Hall plateau in R_{xy} (not shown) in the 6.9 to 300 mK temperature range. Thus, in our sample there is no evidence for the formation of any FQHS in the TLL.

We find that the temperature evolution of R_{xx} of the RIQHS in the TLL and that of RIQHSs in the SLL share the following common features: at the lowest temperatures there are two well separated spikes of finite resistance flanking the vanishing R_{xx}, with increasing T these two spike merge into a single peak, and this peak dissapears into a smooth background with a further increase in T. Such a temperature dependence for the $R4a$ state of the TLL is shown in Fig 4.2. We define the center of a RIQHS as the location ν_c at which the extent of the vanishing R_{xx} plateau is nearly
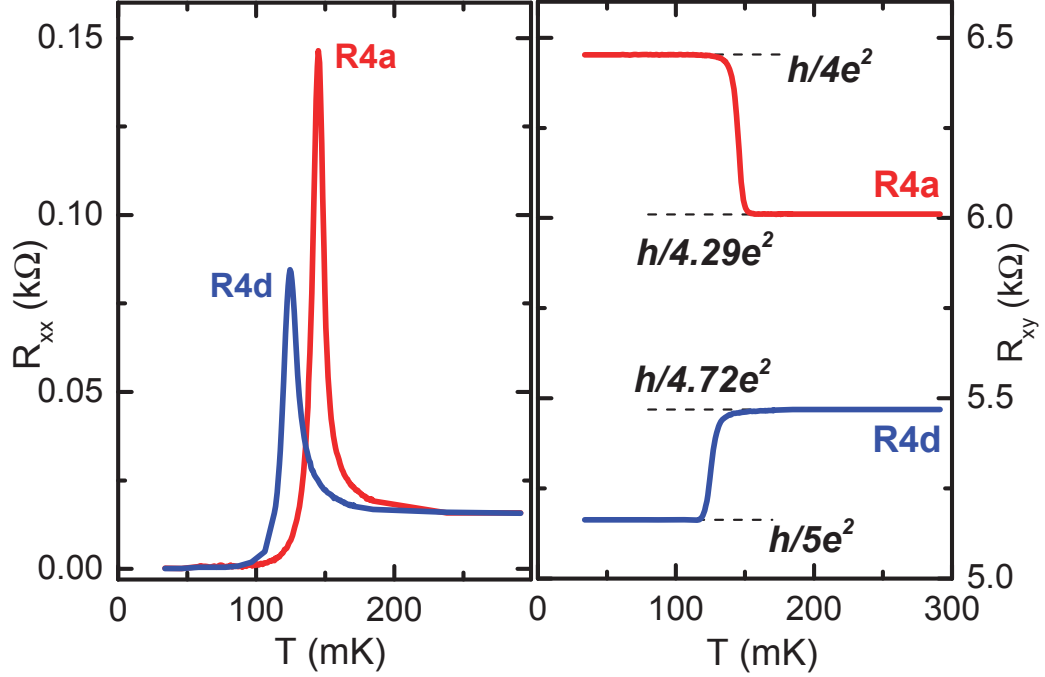
Figure 4.3. The magnetoresistance R_{xx} and the Hall resistance R_{xy} of two RIQHSs in the lower spin branch of the third Landau level measured at $\nu = 4.29$ and $\nu = 4.72$. This data is published in Ref. [114]

zero. For example, the curve at 128 mK of Fig 4.2 exhibits a $R4a$ state of nearly zero width at $\nu_c = 4.287$. The partial filling factor ν_c^* is the decimal part of ν_c, and values for the various RIQHSs are summarized in Table 4.1.

A second shared feature of the RIQHSs in the TLL and in the SLL is the similar R_{xx} and R_{xy} versus T curves measured at a fixed ν. In Fig 4.3 we show such curves for the $R4a$ and $R4d$ states of the TLL in close vicinity to their respective central filling factors. As the temperature is increased the Hall resistance undergoes an extremely abrupt change from the nearest integer quantized value to the classical Hall value $B/ne = h/\nu e^2$. Simultaneously with the sharp change in R_{xy} the longitudinal resistance R_{xx} for the $R4a$ state exhibits a sharp peak of width at half height of

only 10 mK. We have recently reported similar dependences of both R_{xy} and R_{xx} of the RIQHSs in the SLL of a higher density sample and have interpreted the peak temperature as the onset temperature T_c of the RIQHSs. We thus find that a peak in the R_{xx} versus T curves accompanied by a sharp transition of R_{xy} from the classical Hall to a quantized value is not specific to the SLL, but is also a property of the RIQHSs forming in the TLL.

The R_{xx} and R_{xy} versus T curves for the $R3a$, $R3b$, $R3c$ and $R3d$ states of the upper spin branch of the SLL are also shown in Fig 4.4 while those for the $R5a$ and $R5d$ states of the upper spin branch of the TLL are shown in Fig 4.5.

4.3   Contrasting Energy Scales

As we mentioned in the beginning, there are severe differences between RIQHSs in the SLL and TLL which need to be quantatively examined.

We firstly compare the locations, i.e. the filling factors of the RIQHSs. Surprisingly, the filling factors of the RIQHSs in the TLL have not yet been measured with high precision [23–25, 30]. Inspecting Table 4.1 we find that $R2a$, $R3a$ from the SLL and $R4a$, and $R5a$ from the TLL develop at similar partial filling factors. Indeed, $\nu_c^*|_{R3a} = \nu_c^*|_{R4a} = \nu_c^*|_{R5a}$ within our measurement error of ± 0.003. Furthermore, this common value is in close proximity to $\nu_c^*|_{R2a}$. Nonetheless, we measure a significant

Table 4.1
Central filling factors ν_c^* and onset temperatures T_c of the RIQHSs measured.

	$R2a$	$R2b$	$R2c$	$R2d$	$R3a$	$R3b$	$R3c$	$R3d$
ν_c^*	0.300	0.438	0.568	0.700	0.288	0.430	0.576	0.713
T_c[mK]	45.3	29.8	39.9	29.5	38.1	25.4	31.0	25.5
	$R4a$	$R4d$	$R5a$	$R5d$				
ν_c^*	0.287	0.714	0.286	0.714				
T_c[mK]	145	125	111	100				
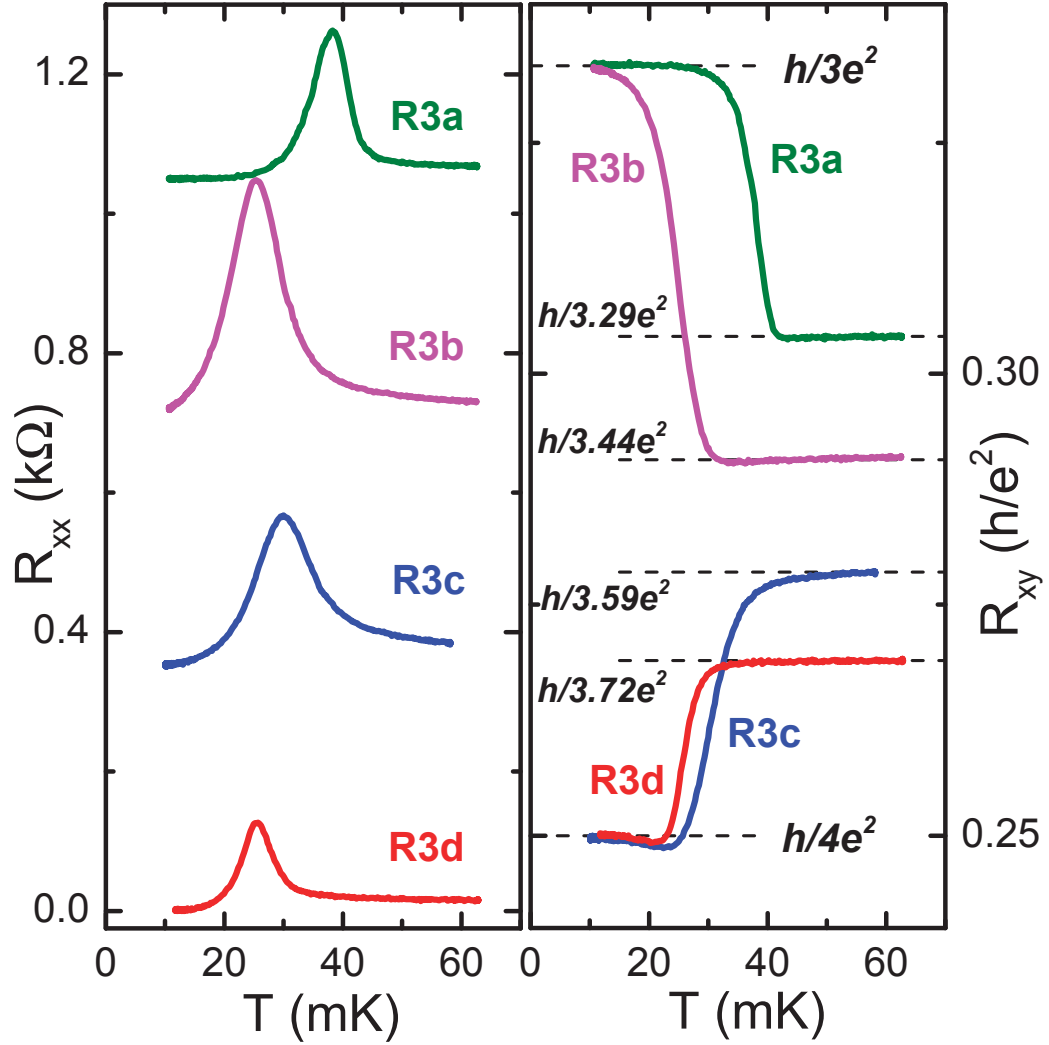
Figure 4.4. The magnetoresistance R_{xx} and the Hall resistance R_{xy} of four RIQHSs in the upper spin branch of the second Landau level measured at $\nu = 3.29$, $\nu = 3.44$, $\nu = 3.59$ and $\nu = 3.72$. (Unpublished data)

difference between the common value of $\nu_c^*|_{Ria}$, with $i = 3, 4, 5$ and $\nu_c^*|_{R2a}$. This is seen in Fig 4.6 as an alignment of data points associated with $R3a$, $R4a$, and $R5a$ onto a vertical dashed line and a slight horizontal departure of the point associated with $R2a$ from this line. A similar alignment occurs for the particle-hole symmetric states
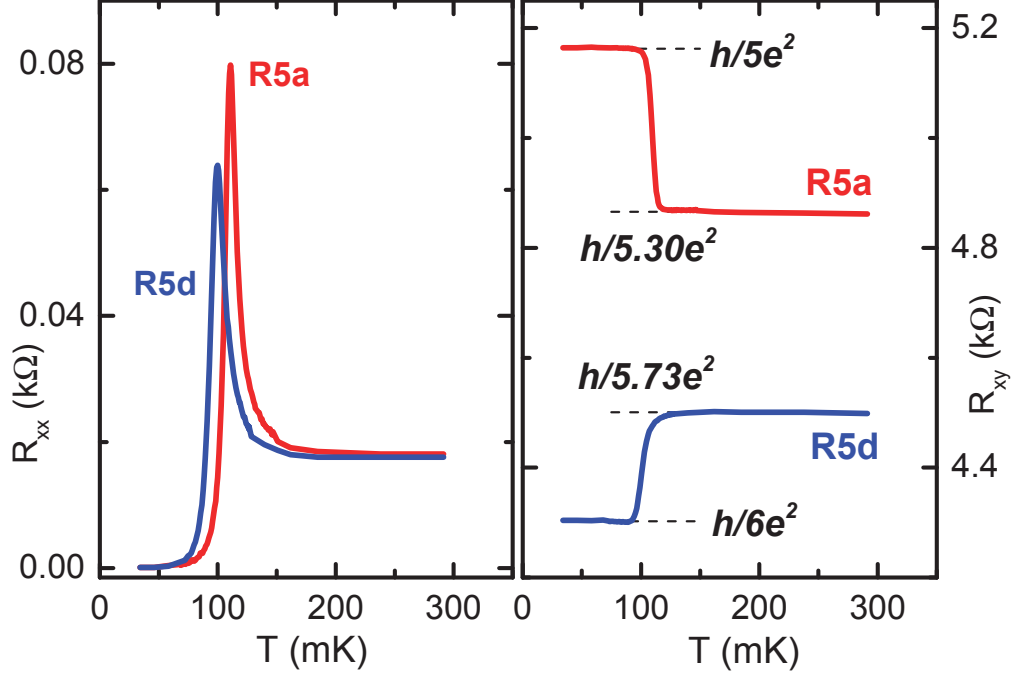
Figure 4.5. The magnetoresistance R_{xx} and the Hall resistance R_{xy} of two RIQHSs in the upper spin branch of the third Landau level measured at $\nu = 5.30$ and $\nu = 5.73$. (Unpublished data)

R2d, R3d, R4d, and R5d. We summarize thus that RIQHSs Ria with $i = 2, 3, 4$ and 5 form at similar partial filling factors and yet theory favors different types of order for these states: one-electron bubbles or WS at R2a and R3a [29] and two-electron bubbles for R4a and R5a [27–29, 63, 65].

As a further test we examine the energy scales of the RIQHSs. The cohesive energy of the bubble phase E_{coh} is readily obtained from the Hartree-Fock theories [22, 29, 63, 65, 66]. It is customary to calculate the reduced cohesive energy $e_{\mathrm{coh}} = E_{\mathrm{coh}}/E_c$, where $E_c = e^2/4\pi\epsilon l_B$ is the Coulomb energy and $l_B = \sqrt{\hbar/eB}$ the magnetic length. Experimentally we measure the onset temperature T_c and we consider the reduced onset temperature $t_c = k_B T_c/E_c$. Fig 4.6 summarizes the t_c of the RIQHSs in the SLL and TLL as function of ν_c^*. We assume that, within the bubble interpretation,
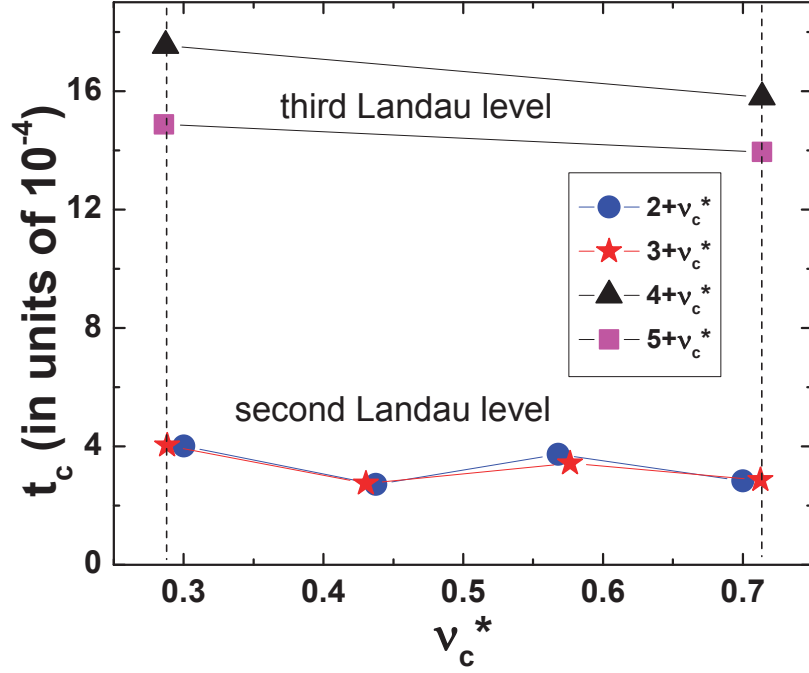
Figure 4.6. The reduced onset temperatures $t_c = k_B T_c / E_c$ of the RIQHSs in the SLL and TLL plotted as function of the partial filling factor ν_c^*. Lines are guides to the eye. This data is published in Ref. [114]

the onset temperature of a RIQHS is a measure of its cohesive energy [67]. We find that the reduced onset temperatures t_c of the RIQHSs in the SLL and TLL are more than 2 orders of magnitude smaller than the reduced cohesive energies $e_{\mathrm{coh}} = E_{\mathrm{coh}} / E_c$ of the associated bubble phases [22, 29, 63, 65, 66]. We think this difference is most likely due to disorder and Landau level mixing effects which are not included in the Hartee-Fock estimations [22, 29, 63, 66]. Furthermore, similarly to the results in previous chapter, in the SLL we find a good collapse of t_cs from different spin branches and a non-monotonic dependence of t_c of ν_c^*. As shown in Fig 4.6, t_c in the TLL is in the vicinity of 16×10^{-4}, but the collapse of values from the two different spin branches is not as good as for the RIQHSs in the SLL.

Our most remarkable finding is the disproportionately large energy scales of the RIQHSs in the TLL as compared to those in the SLL. The most striking disagreement is between the RIQHSs $R4a$ and $R2b$ believed to be two-electron bubbles. The theory predicts similar cohesive energies $e_{\text{coh}}^{R4a}/e_{\text{coh}}^{R2b} \approx 1.2$ [29]. In contrast to these predictions, we measure a large difference in the onset temperatures $t_c^{R4a}/t_c^{R2b} = 6.4$. We also find $e_{\text{coh}}^{R4a}/e_{\text{coh}}^{R2a} \approx 1$ [29], while we measure $t_c^{R4a}/t_c^{R2a} = 4.3$. Taken together, we conclude that there are clear quantitative inconsistencies between the measured and calculated energy scales of the RIQHSs. We note that, within the SLL, the measured and theoretical energy scales of $R2a$ and $R2b$ states compare surprisingly well: $t_c^{R2a}/t_c^{R2b} = 1.5$ and $e_{\text{coh}}^{R2a}/e_{\text{coh}}^{R2b} \approx 1.2$ [29].

One scenario which could account for our onset temperature data is that, contrary to the theory [29], all of the RIQHSs in the SLL are bubble phases of the same type and those in the TLL are bubbles of a different kind. We cannot, however, discard the possibility that the RIQHSs of the second and third LLs are the same type of bubble phases. The large difference in onsets could be caused by an effect dependent on LL occupancy. Because of the presence of one extra filled LL, screening of the disorder potential in the TLL is expected to be more effective than that in the SLL [22, 73]. The substantially larger onsets of the RIQHSs in the TLL as compared to those in the SLL could thus be a consequence of a smoother effective disorder potential due to screening of one extra filled LL.

Finally we note that there are two recent reports of reentrant behavior in the lowest LL in 2DEGs forming in GaAs/AlGaAs hosts. One such observation is made in a heterostructure which has short range neutral scattering centers [101]. Another experiment was performed on wide quantum wells [68]. In both of these experiments reentrance has been associated with the formation of electron solids similar to the WS since electron-electron interactions in the lowest LL are not expected to promote electronic bubble phases [63]. However, the relationship between these electron solids and those in higher LLs we have studied is not understood at this time.

4.4 Conclusions

To conclude, the reported common features in the transport of the RIQHSs both in the TLL and SLL, together with the reentrant behavior and radiofrequency response, support the idea that the RIQHSs belong to the same family of ground states, irrespective of the LL they form in. These features are qualitatively consistent with the bubble interpretation of these phases. We found, however, that the very different energy scales of the RIQHSs in different LLs are inconsistent with quantitative predictions of the theory of the bubbles. This disagreement is suggestive of an assignment of the RIQHSs to bubble phases different than that proposed by the theory. Our results call for further work in order to elucidate the nature of the RIQHSs.

5. ORBITAL DEPENDENCE OF THE REENTRANT INTEGER QUANTUM HALL STATES

In previous two chapters, I have discussed the reentrant integer quantum Hall states (RIQHS) in both the second Landau level ($N = 1$) and the third Landau level ($N = 2$). The RIQHSs are not only developing in the first two excited Landau levels (LL), but can develop in much higher Landau levels. In fact, the ground states of RIQHSs, i.e. the bubble phases were historically predicted in high Landau level limit [22, 66]. However, in current dc as well as microwave transport experiments on RIQHSs, the highest Landau level being measured is only the lower spin branch of the fourth or $N = 3$ Landau level [23, 24, 30, 31]. Therefore, there is a lack of data to study how these electron solids evolve with different Landau levels. For instance, the Landau level dependence of the number of electrons per unit cell remains largely unknown.

Furthermore, as mentioned in the introduction, there is very little work in understanding finite temperature behavior of the RIQHSs. The peaks we have observed in the temperature dependence of the RIQHSs indicate an unusual melting mechanisms of these special electron crystals [74]. Interestingly, a recent experimental and theoretical study of the RIQHSs in the third Landau level ($N = 2$) claims that the topological defects play an important role in the melting [34]. It therefore raises an question whether such a theory can be generally applied to other RIQHSs both in the second Landau level and in even higher Landau levels.

In this chapter we study the temperature dependent magnetoresistances of fully developed RIQHSs in Landau levels of $N = 1, 2, 3$ and 4. The capability of preparing RIQHSs in Landau level as high as $N = 4$ in our system enables an examination of the evolution of RIQHSs with Landau levels. Combining with our previous data of RIQHSs in the $N = 1$ and the $N = 2$ Landau levels, we find the sharp peaks are

universally present in the temperature dependent longitudinal resistance of RIQHSs in all four Landau levels. By utilizing these peaks, we can extract onset temperature T_c to characterize the energy scales of their ground states. We find an intriguing trend of T_c that it changes smoothly within each LL but increases abruptly at the transitions between successive Landau levels. More strikingly, in scales of cyclotron energy, the reduced T_c is nearly independent of ν within each Landau level but strongly depends on the Landau level index N. We interpret such a function of reduced T_c versus N to be the first evidence of the Landau level dependence of the internal structures of bubble phases. Further comparison between the Landau level dependence of T_c and cohesive energy predicted in Hartree-Fock theory indicates the melting of RIQHSs is unusual which can not be simply explained by thermal dislocation in crystal phases.

5.1 Magnetotransport Signatures Of Reentrant Integer Quantum Hall States In High Landau Levels

The sample we used in this study is the same as the one in which we contrast the energy scales of the $N = 1$ and $N = 2$ Landau levels. In Fig 5.1 we plot the longitudinal resistivity R_{xx} and Hall resistivity R_{xy} of the sample against B field (bottom scale) and $\nu = nh/eB$ (top scale) measured in a filling facotr range of $4 < \nu < 10$ at 58 mK. In this filling factor range, there are three Landau levels: the $N = 2$ LL spans $4 < \nu < 6$; the $N = 3$ LL spans $6 < \nu < 8$; and the $N = 4$ LL spans $8 < \nu < 10$. Due to the large B field, each Landau level contains two split spin branches. There are two types of quantum Hall ground states identified in these high LLs by their well-defined features in Hall resistivity R_{xy}. The first one is the integer quantum Hall state (IQHS) with Hall plateau centered at each integer i. At $\nu = i$, the quantization of corresponding plateau accurately assumes the value h/ie^2. The second one is the reentrant integer quantum Hall states associated with the other Hall plateaus which do not cross any integer [23,24]. Away from each $\nu = i$, the R_{xy} firstly deviates towards the classical Hall line and then returns to such plateaus quantized
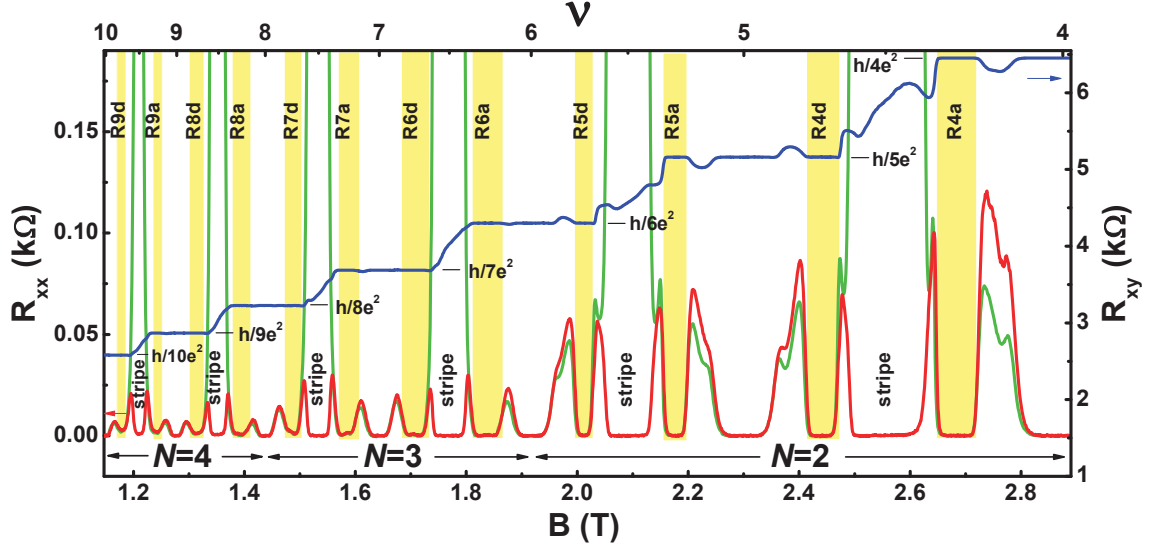
Figure 5.1. The magnetoresistances in the third ($4 < \nu < 6$), the fourth ($6 < \nu < 8$) and the fifth ($8 < \nu < 10$) Landau levels are measured at 58 mK with RIQHSs in shaded regions. The R_{xx} traces are longitudinal resistivity measured in mutually perpendicular crystal axes [110] and [1$\bar{1}$0]. This data is taken from Ref. [116]

exactly at h/ie^2. Simultaneously, the Hall plateaus in both IQHS and RIQHS is accompanied by vanishing R_{xx}. For example, the RIQHS labeled $R4a$ in the $N = 2$ LL shows a Hall plateau and vanishing R_{xx} centered at $\nu = 4.287$ which is separate from those of the IQHS at $\nu = 4$. We note that in the $N = 3$ and $N = 4$ LLs the separation of the Hall plateaus of neighboring IQHS and RIQHS is less discernible while a distinct peak in R_{xx} still separates them. The RIQHSs are shaded green and labeled as $R4a$, $R4d$, $R5a$, $R5d$ in the $N = 2$ LL, $R6a$, $R6d$, $R7a$, $R7d$ in the $N = 3$ LL and $R8a$, $R8d$, $R9a$, $R9d$ in the $N = 4$ LL. The well developed reentrant features in the Landau level as high as $N = 4$ demonstrate very high quality of this sample. Besides the RIQHSs, the stripe phases are also identified by their large anisotropy in R_{xx} measured in perpendicular crystal axes [110] and [1$\bar{1}$0] and shaded in yellow in Fig 5.1 [23, 24].
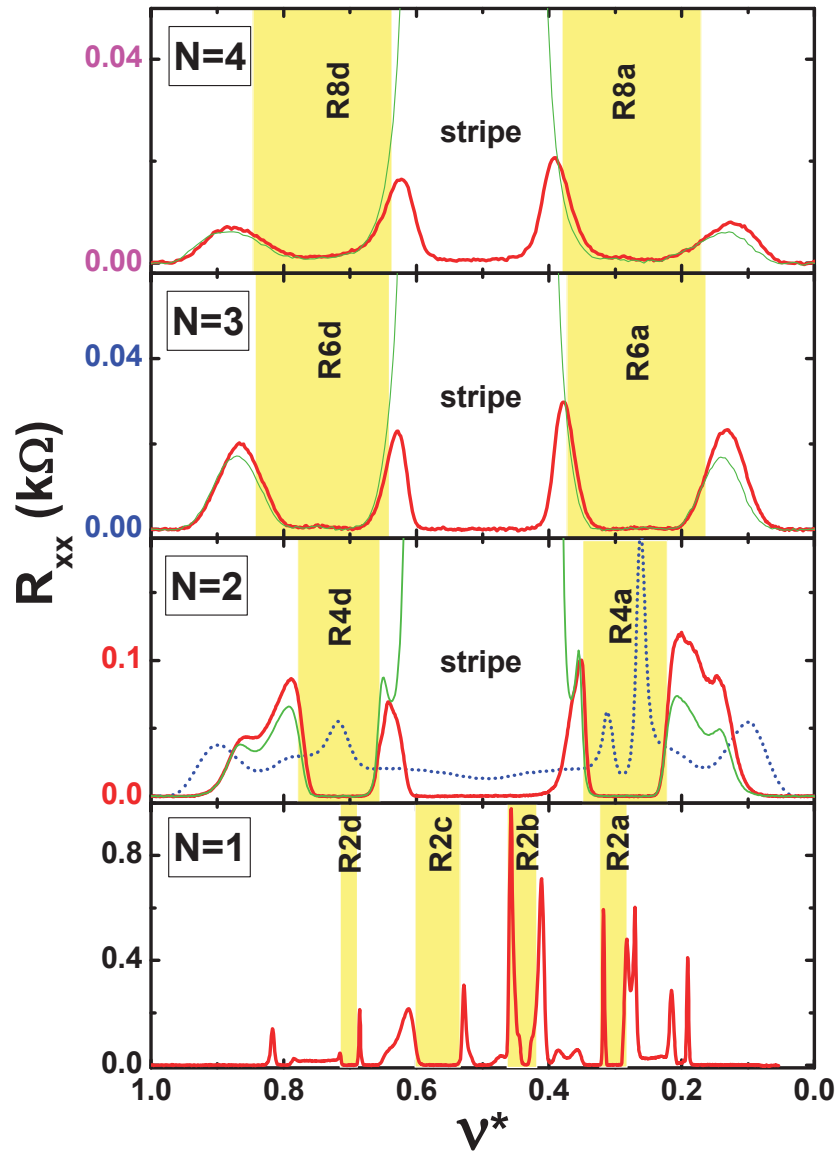
Figure 5.2. A comparison of the magnetoresistance of the lower spin branch between $N = 1$ at 6.9 mK and $N = 2, 3$, and 4 Landau levels at 58mK. Dotted trace in $N = 2$ Landau level is measured at 128mK, showing the typical evolution of the R_{xx} with respect to temperature. This data is taken from Ref. [116]

Fig 5.2 shows a direct visualization of the filling factors of RIQHSs in different Landau levels from $N = 1$ to $N = 4$. Since the RIQHSs in the $N = 1$ LL develop

at much lower temperture, the trace of $N = 1$ LL was taken at 6.9 mK while those of $N = 2, 3,$and 4 were taken at 58mK. For simplicity due to particle-hole symmetry, only the lower spin branch of each Landau level is plotted against the partial filling factor ν^* where ν^* is the fractional part of ν. From Fig 5.2, we clearly observe that the filling factors of $R2a$, $R4a$, $R6a$ and $R8a$ overlap with each other around $\nu^* = 0.3$, indicating a similar origin of bubble phase. The filling factors of their particle-hole conjugate states $R2d$, $R4d$, $R6d$ and $R8d$ overlap around $\nu^* = 0.7$. In the $N = 1$ LL, however, there are two extra RIQHSs $R2b$ and $R2c$ while in higher Landau levels the corresponding filling factors are occupied by stripe phases. While Hartree-Fock theory predicts the same two-electron bubble phase in the $R2b$ and $R4a$ but one-electron bubble phase in the $R2a$ [29], our comparisons of their energy scales reveal a contradiction to this assignments. Indeed, the energy scale of $R4a$ is found to be five times larger than those of $R2a$ and $R2b$ which share similar values. Accordingly, we propose a different scenario that all RIQHSs in the $N = 1$ LL are bubble phases of the same type and those in the $N = 2$ LL are bubble phases of a different kind.

5.2 Evolution Of Transport Signatures With Landau Levels

We have established a generic evolution pattern of R_{xx} with temperature T for the RIQHSs in both $N = 1$ and $N = 2$ LLs. At the lowest temperature, there are two spikes of finite resistance flanking the vanishing R_{xx}. With increasing T, the two resistance spikes move towards each other and the vanishing region of R_{xx} turns into a local minimum. Such a minimum is shown in the dotted trace of elevated $T = 128$mK in the $R4a$ in Fig 5.2. We define the filling factor at the minimum as the central filling factor ν_c of corresponding RIQHS. As T increases further, the two resistance spikes merge into a single peak and the single peak disappears rapidly into a smooth background at higher T. For the RIQHSs in the $N = 3$ and $N = 4$ LLs, we observe similar temperature evolution pattern in their R_{xx} so that exact ν_cs can be measured for the total eight RIQHSs and are summarized in Table 5.1. Additionally,
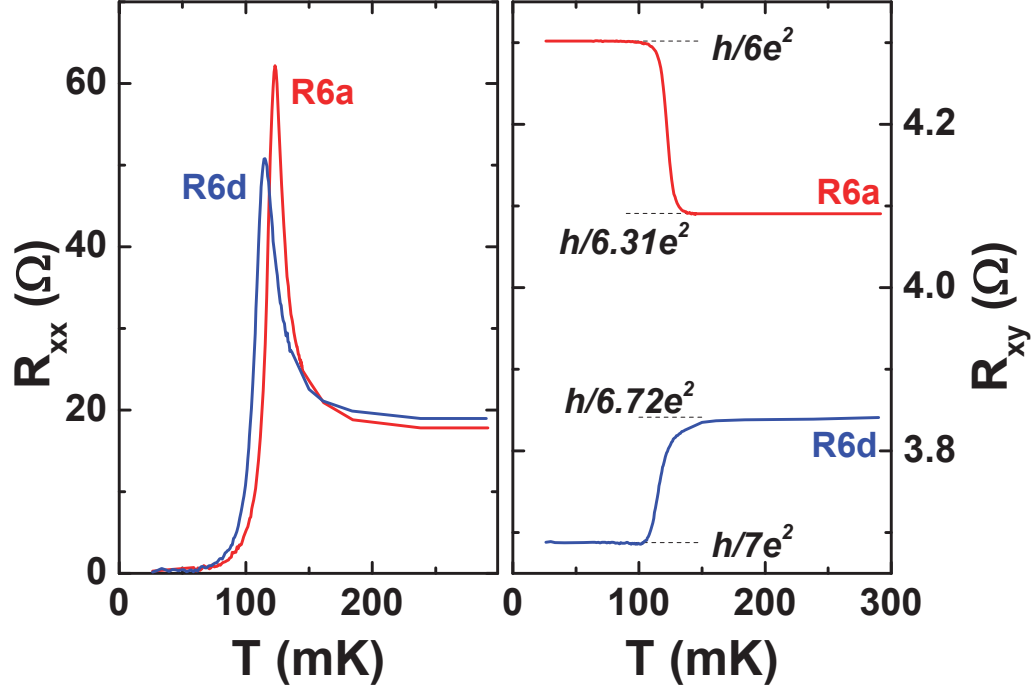
Figure 5.3. The magnetoresistance R_{xx} and the Hall resistance R_{xy} of two RIQHSs in the lower spin branch of the $N = 3$ Landau level measured at $\nu = 6.31$ and $\nu = 6.72$. This data is taken from Ref. [116]

the T-dependent R_{xx} in RIQHSs in the $N = 3$ LL has demonstrated more complex features which are discussed in the end.

The temperature evolution pattern can be equivalently demonstrated by performing temperature scans at any fixed ν in the RIQHSs. Fig 5.3 shows both R_{xx} and R_{xy} versus T for the $R6a$ and $R6d$ in the $N = 3$ LL at ν near their respective central filling factors. As the temperature increases, we observed a sharp change in R_{xy} from integer quantized value to the classical Hall value $B/ne = h/\nu e^2$. Simultaneously, with the sharp change in R_{xy}, a peak of width at half height of only 15 mK is observed in R_{xx} for the $R6a$. Such a peak has been a unique signature of RIQHS and has not been demonstrated in the temperature dependence of any IQHS or FQHS. Similar

curves for the $R7a$ and $R7d$ states in the upper spin branch of the $N = 3$ LL are also shown in Fig 5.4.
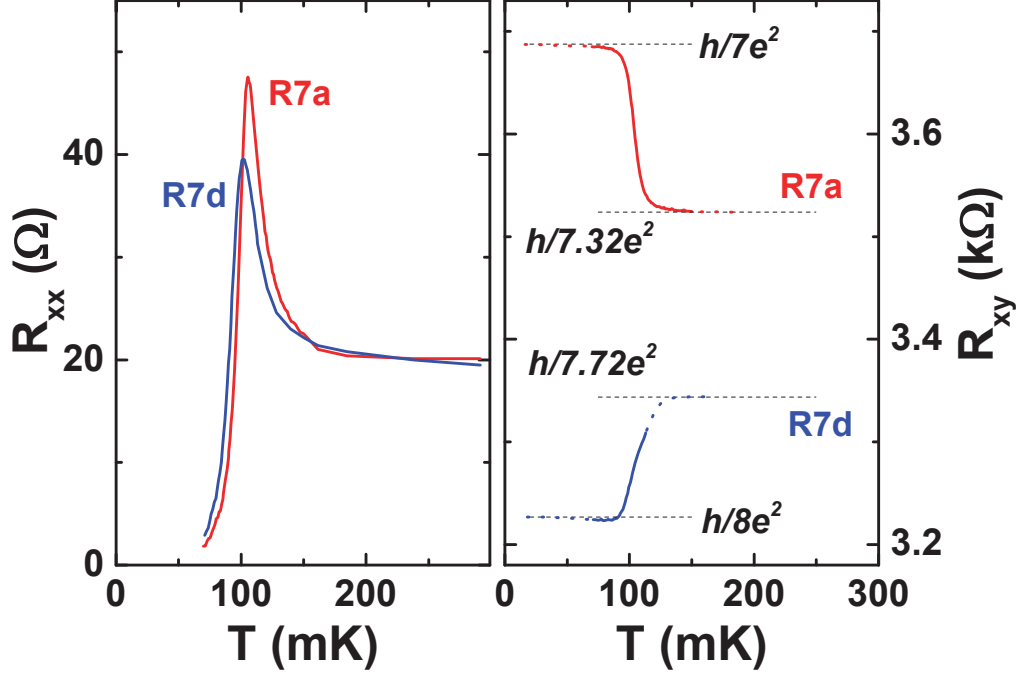
Figure 5.4. The magnetoresistance R_{xx} and the Hall resistance R_{xy} of two RIQHSs in the upper spin branch of the $N = 3$ Landau level measured at $\nu = 7.32$ and $\nu = 7.72$. The dots in the R_{xy} on the right panel are not experimental data but extrapolation of the solid curve.

In order to study the evolution of this peak signature with respect to the Landau level, we include in Fig 5.5 similar data measured in the $N = 1$ and $N = 2$ LLs. For clarity, only the first RIQHS in each Landau level, namely $R2a, R2b, R2c$ and $R2d$, are selected to show in the Fig 5.5. From Fig 5.5, we find that RIQHS in the $N = 1$ LL is obviously distinct from the RIQHSs in higher Landau levels in terms of very low T_c as well as the narrowest peak of width at half height of only 5 mK. Such an extremely sharp peak indicates a first-order transition from crystal phase to liquid phase which agrees with the findings from recent thermoelectric study of the

RIQHSs in the $N = 1$ LL [74]. In the $N \geq 1$ LLs, with increasing LL index N, T_c consistently decreases while the width of the peak is broadened. By viewing their peak signatures as the thermal resonances of the bubble phases, the broadening of the peak may suggest a less rigid crystal or increased sensitivity of these crystals to disorder with increasing Landau levels [65].
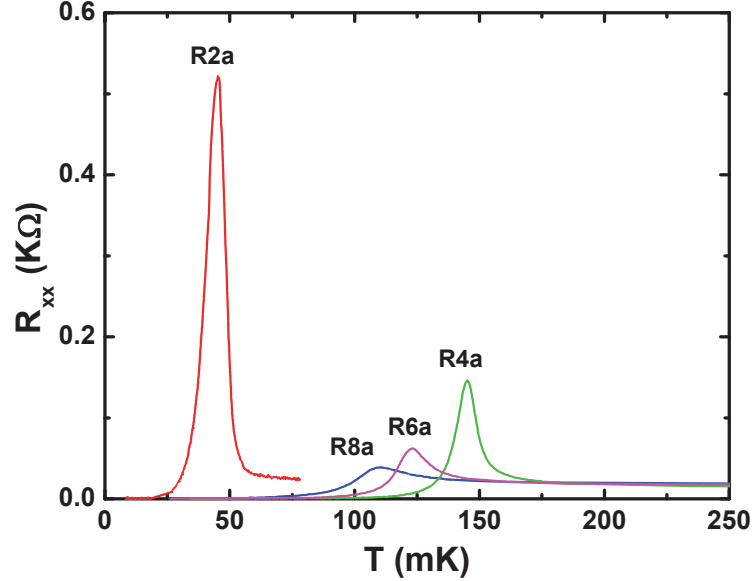
Figure 5.5. The temperature dependence of magnetoresistance measured near the center ν_c of reentrant states $R2a$, $R4a$, $R6a$, $R8a$. This data is taken from Ref. [116]

The T-dependent R_{xx} at fixed filling factor near ν_c allows us to extract the onset temperature T_c with high precision. T_c is defined at the peak which corresponds to the transition temperature from the bubble phases to the classical electron liquids. We summarize the values of T_c measured in the $N = 3$ and $N = 4$ LLs in Table 5.1 while those in the $N = 1$ and $N = 2$ LLs can be found in Table 4.1 in previous chapter. We plot T_c measured near ν_c against magnetic field for the RIQHSs in all four Landau levels in the Fig 5.6. We find that T_c decreases nearly linearly with increasing B_c within each LL except for a relatively large fluctuation of T_c in the $N = 1$ LL which contradicts the particle-hole asymmetry. Between successive LLs,

however, there is an abrupt change of T_c. For instance, from $N = 2$ to $N = 3$ LL, T_c of the $R6a$ at $B_c = 1.825$T has a sudden increase of 23 mK compared with T_c of the $R5d$ at $B_c = 2.013$T. Such a discontinuity at successive Landau levels clearly shows a strong Landau level dependence of T_c.
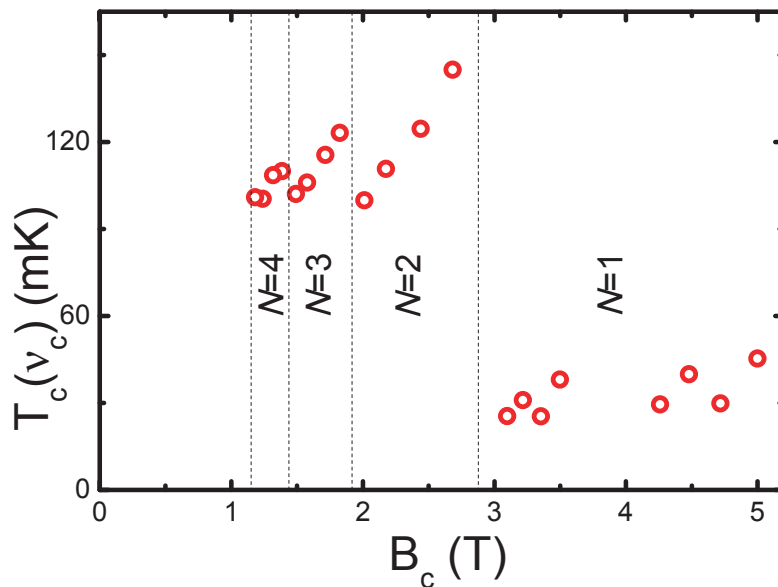
Figure 5.6. Onset temperature T_c measured near the center filling factor ν_c of each RIQHS. The T_c is plotted against the magnetic field. This data is taken from Ref. [116]

Table 5.1

Center filling factors ν_c and onset temperatures T_c of RIQHSs in the fourth and the fifth LLs.

	$R6a$	$R6d$	$R7a$	$R7d$	$R8a$	$R8d$	$R9a$	$R9d$
ν_c	6.302	6.703	7.298	7.709	8.299	8.727	9.283	9.731
$T_c(\nu_c)$	123	116	106	102	110	109	100	101

5.3 Landau Level Dependence Of The Energy Scales Of Reentrant Integer Quantum Hall States

In the following, we analyze the energy scales of the RIQHSs by using their onset temperatures T_c. We assume that under bubble phase interpretation, the T_c can be used as a measure of the cohesive energy predicted by theory. We note that the theoretical study of cohesive energy in high Landau level limit adopts a characteristic energy unit of cyclotron energy $E_{cyc} = \hbar eB/m^*$ where $m^* = 0.067m_e$ is the effective electron mass in GaAs. Surprisingly, after scaling T_c with E_{cyc} in Fig 5.7a, we find it is nearly independent of ν within each Landau level but depends strongly on the Landau level index N. This is consistent with the linearity of T_c against B_c within each LL observed in the inset of Fig 5.6. Such a scaling with E_{cyc} is clear in $N \geq 1$ Landau levels which indicates the particle-hole symmetry of the four RIQHSs is preserved. In the $N = 1$ Landau level, however, we found T_c scales better with Coulomb energy and reported a particle-hole asymmetry. One possible explanation for this difference given by Ref. [63] is that in high Landau levels ($N \geq 1$) the length scale of the crystal ground state is determined by cyclotron radius of valence LL electrons instead of the magnetic length. Consequently, the new length scale sets an effective Coulomb energy which is proportional to the cyclotron energy. However, we cannot rule out the other possibility that the melting mechanism of RIQHSs in the $N = 1$ LL is fundamentally different than that of the RIQHSs in higher LLs and T_c measured in $N = 1$ LL scales with a different energy scale.

To better understand the Landau level dependence of T_c/E_{cyc}, we average T_c/E_{cyc} over each LL and plot it against N in Fig 5.7b. An increasing trend of T_c/E_{cyc} with respect to N can be obviously seen in this dependence and it is opposite to the predicted dependence of cohesive energy in the large N limit [22]. Such a disagreement between experiment and theory is puzzling and may result from several possibilities. One is that our highest measured Landau level is still much under the theoretical high Landau level limit and hence can not be captured by Hartree-Fock approximation.

Second, the Hartree-Fock models do not consider the effects of disorder or LL mixing which can have great impacts on the energy scales of many-body states such as FQHSs. Despite of the disagreement, our data rigorously shows a strong Landau level dependence of the energy scales of RIQHSs. This Landau level dependence may indicate that the internal structure of RIQHS (specifically number of electrons per bubble) changes with Landau levels, contributing to their different energetics.

We note that a recent study suggests a very unique melting mechanism of bubble phases which may account for the peak signature observed in our temperature dependence measurements of RIQHSs [34]. Instead of classical melting due to dislocation, the topological defects in the bubble phases can lead to an early onset of the melting with increasing temperature. Quite remarkably, this theory predicts an onset temperature of about 100 mK for the RIQHSs in the $N = 2$ LL which is in the range of our measured values. However, to establish this theory in other RIQHSs, similar calculations of T_c in other Landau levels are need to compare with our data.

Finally we have observed a possible phase split in the RIQHSs of $N = 3$ LL. Fig 5.7 shows the temperature dependence of R_{xx} for the $R6a$ of the $N = 3$ LL as an exemplary case. Similar to the lowest temperature features of RIQHSs in the $N = 1$ and $N = 2$ LLs, only one vanishing region of R_{xx} is flanked by two spikes at 58 mK. However as T is increased by 20 mK, a new spike marked c emerges at $\nu = 6.246$ while the original two spikes evolve into a and b. We interpret the new spike as a separation of reentrant regions that they corresponds to two different bubble phases. The split-off RIQHS centered around a different ν_c 6.227 is labeled $R6\tilde{a}$ and the two RIQHSs are shaded accordingly. The subsequent temperature dependence of both $R6a$ and $R6\tilde{a}$ follow the established evolution pattern of RIQHSs in the $N = 1$ and $N = 2$ LLs. As to $R6a$, the merging of two spikes into a single peak can be clearly seen in the trace of 121 mK. Since $R6\tilde{a}$ is much weaker than $R6a$, however, the expected single peak is obscured by the high resistance background of $R6a$. Quite interestingly, we note that the Hartree-Fock theory indeed predicts two different bubble phases in the
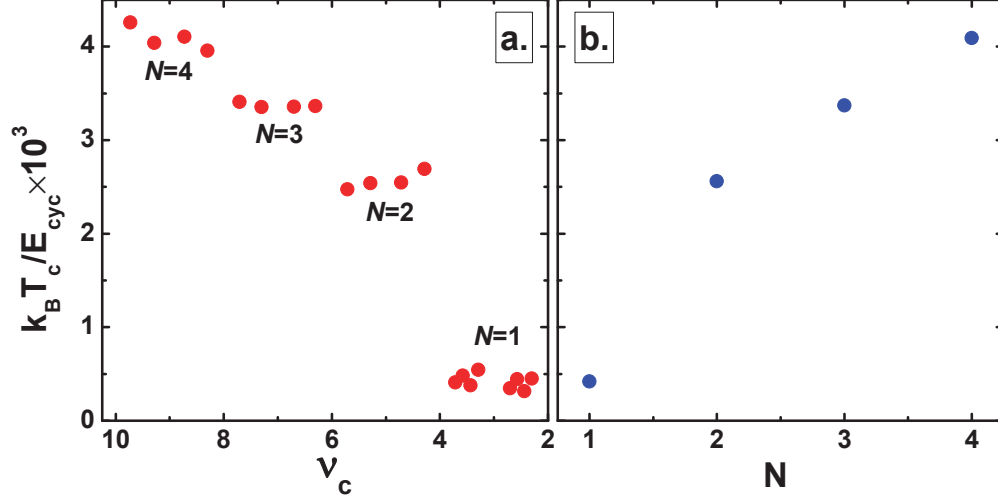
Figure 5.7. The onset temperature $T_c(\nu_c)$ scaled with cyclotron energy (panel a) plotted against filling factor ν and its average over each Landau level (panel b) is plotted against the corresponding Landau level index N. This data is taken from Ref. [116]

$N = 3$ LL. The temperature dependence of RIQHSs of the $N = 3$ LL are reminiscent of a phase split reported in the $R2a$ of $N = 1$ LL [45].

5.4   Conclusions

To sum up, in this chapter, I study the RIQHSs in the fourth and the fifth Landau levels. By including the data in the second and the third Landau level, a strong Landau level dependence of the energy scales of RIQHE is found. Their energy scales normalized by cyclotron energy shows nearly no dependence on filling factors within each Landau level but strong dependence on the Landau orbital index N. Such a clear Landau orbital dependence is likely associated with different microscopic structures

69
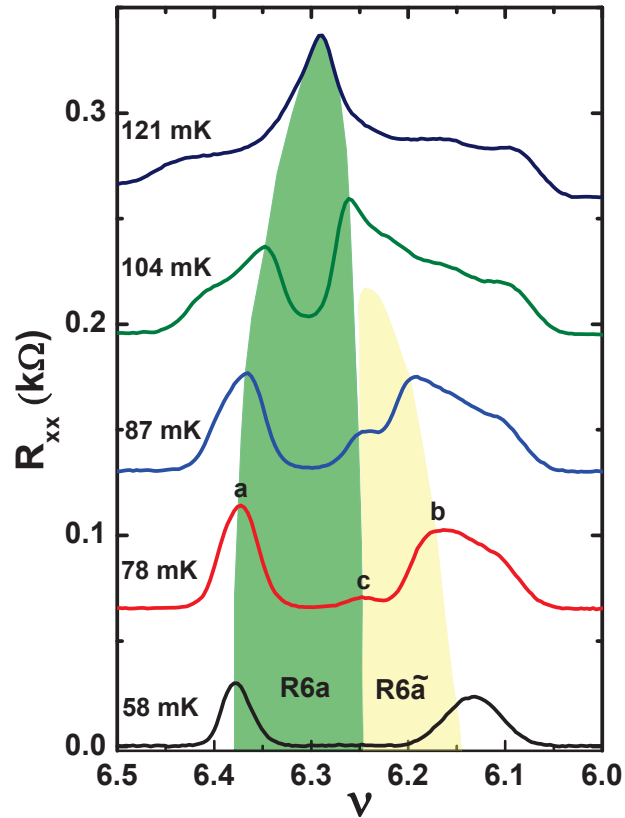
Figure 5.8. The evolution with temperature of the $R6a$ in the fourth Landau level. Traces are shifted by 70Ω for clarity. The green and yellow shaded regions represent two reentrant states of different temperature dependence. This data is taken from Ref. [116]

of bubble phases predicted in different Landau levels. Furthermore, a comparison of our data and Hartree-Fock theory hints an unusual melting mechanism of these intricate bubble structures and provides inputs to its understanding.

6. THE $\nu = 5/2$ FRACTIONAL QUANTUM HALL STATE IN THE PRESENCE OF ALLOY DISORDER

While in previous three chapters I have reported the study of reentrant integer quantum Hall states in many different Landau levels, I will turn to discuss our experiments in the same system of two dimensional electron gas but on a different topic: how disorder in our samples affect the exotic $\nu = 5/2$ fractional quantum Hall state (FQHS) in the second Landau level.

In the temperature regimes of fractional quantum Hall states, the acoustic phonon scattering of electron is negligible. The low temperature electron scattering in a high quality GaAs/AlGaAs samples are mainly due to the disorder introduced during growth such as the remote ionized silicon donors, unintentional background impurity or interface surface roughness [38]. The ionized silicon donors are randomly distributed in a thin layer at a setback distance from the quantum well and can create fluctuating Coulomb potential. Such a disorder potential has a relatively long range with a length scale set by the setback distance of ~100nm. The unintentional background impurity can be either charged or neutral and are uniformly distributed in the GaAs/AlGaAs lattice. Although it has a low concentration on the order of $10^{13}/\text{cm}^2$ in the best samples, it can have more influence on the electrons in the quantum well. In fact, in the state-of-the-art samples grown by MBE, the unintentional background impurity becomes the dominant disorder mechanism [38]. It has been predicted that electron mobility will exceed $100 \times 10^6 \text{cm}^2/\text{Vs}$ if the concentration of unintentional background impurity is below $10^{12}/\text{cm}^2$ [75]. Finally, the surface roughness at the interface of the quantum well is usually modeled as neutral and short range disorder of sub-nanometer length scale. Similarly, the neutral unintentional background impurity also has a short range but strong scattering potential. This short range dis-

order potential is responsible for the large-angle scattering of the electrons compared with the small-angle scattering due to a slow varying, long range Coulomb disorder potential.

In general, the disorder effects on single particle states are well understood. Examples of fundamental importance are Anderson localization [26] and universal plateau-to-plateau transition in the integer quantum Hall effect [76]. Localization in the presence of the disorder is also important in topological insulators [77] and in atomic condensates [78]. In contrast, understanding disorder in correlated electron systems continues to pose serious challenges. The interplay of disorder and interactions has witnessed renewed interest in the two-dimensional electron gas (2DEG) in connection to the stability of the exotic fractional quantum Hall states [79–81] and in graphene due to the observation of a wealth of FQHSs using local detection [82].

The FQHS at Landau level filling factor $\nu = 5/2$ is one example of a correlated ground state which has attracted considerable attention [8, 25, 35, 36, 39, 45, 47, 49, 51, 83–91]. This is because of the putative exotic Pfaffian-like correlation in the ground state at $\nu = 5/2$ and of the non-Abelian quasiparticle excitations [9, 10, 12]. Non-Abelian quasiparticles may be used to realize topological qubits, building blocks of fault-tolerant quantum computers [19]. Furthermore, since the Pfaffian can be mapped into a paired wavefunction with a p-wave symmetry [9, 10, 15], the $\nu = 5/2$ FQHS is intimately connected to p-wave superconductors [92], Majorana physics in superconductor-semiconductor hybrid devices [93], and superfluid ^{3}He [94].

The effect of the disorder on the $\nu = 5/2$ FQHS remains largely unknown [79–81]. Disorder is a key factor in limiting $\Delta_{5/2}$, the energy gap of the $\nu = 5/2$ FQHS, to less than 0.6 K [36, 39, 83]. Measurements of this state must therefore be conducted at either dilution or nuclear demagnetization refrigerator temperatures, which render these studies time consuming [35, 95]. However, in the disorder-free limit $\Delta_{5/2}$ is predicted to be as high as 2 K at the typical electron density of $n = 3 \times 10^{11}/\text{cm}^2$ [60, 70, 96–98]. Understanding disorder in the $\nu = 5/2$ FQHS is thus expected to lead to an increased energy gap with the following benefits toward fundamental tests of

the nature of this state: a) experiments may be conducted at higher temperatures, possibly in ^{3}He refrigerators, with shorter turn-around times allowing for extensive investigations b) improved signal-to-noise ratio in experiments on nanostructures in which the edge states of the $\nu = 5/2$ FQHS are probed [47,88–90] and c) exponentially enhanced topological protection in qubits [19].

Studies of disorder require the capability of its control. In this Letter we report on a quantitative inquiry of the impact of a specific type of short-ranged disorder, alloy disorder, on the $\nu = 5/2$ FQHS. We investigated a series of specially engineered samples in which all parameters but the alloy disorder remain constant by design [99]. Specifically, we measured $Al_{0.24}Ga_{0.76}As/Al_xGa_{1-x}As/Al_{0.24}Ga_{0.76}As$ quantum wells in which the electrons are confined to the $Al_xGa_{1-x}As$ alloy and which have different values of the aluminum molar fraction x [99]. Since the disorder is added to the electron channel during the Molecular Beam Epitaxy (MBE) growth, it is controlled and precisely quantified. Disorder is found to suppress the energy gap of the $\nu = 5/2$ FQHS. However, to our surprise we find strong $\nu = 5/2$ FQHSs in alloy samples at values of the electron mobility at which this state does not develop at all in the highest quality alloy-free samples. The mobility threshold for the formation of the $\nu = 5/2$ FQHS in the alloy samples is thus much reduced as compared to that in the alloy-free samples. Our results indicate that the engineering of the exotic FQHSs, such as the one at $\nu = 5/2$, is critically dependent on the different length scales of competing disorders present in the 2DEG: the short-range alloy and interface roughness disorder and the long-range Coulomb disorder.

6.1 Impact Of Alloy Disorder On The Magnetoresistance Of The Second Landau Levels

A sketch of the active region of our alloy-free reference sample and of a sample containing alloy disorder are shown in the insets of Fig 6.1. The sample growth procedure and characterization of our samples at $T = 300$ mK can be found in

Ref. [99]. Some important common parameters of the samples are listed as following: 1. the width of the quantum well is 30 nm; 2. the capping GaAs layer is 10 nm thick; 3. the electron gas is 200 nm deep under the sample surface; 4. the setback distance between the dopants and the quantum well is 75 nm on both sides of the well [99]. The alloy content x, electron density n, electron mobility of different samples are summarized in Table 6.1. By varying x between 0.00057 to 0.0046, we estimate the average Al-Al distance within the electron channel of our samples ranges from 5.3-2.7 nm. In comparison, the unintentionally added charged impurities during the MBE growth are estimated to have a concentration of about $10^{13}/\text{cm}^3$, therefore their average separation is close to 0.5 μm [38, 79].

The preparation of the electronic state is the same for each sample. Samples are cooled in our wet dilution refrigerator to about 5 K in the dark. Samples are then heated up to 10 K and are illuminated for 10 minutes with a red light emitting diode (LED). In order to maintain the same conditions for the LED illumination in different measurements, the LED is placed in a similar position with respect to each sample and the same bias current of 1 mA is used. After illumination, the sample is

Table 6.1

A summary of alloy content x, electron density $n(10^{11}/\text{cm}^2)$, mobility $\mu(10^6\text{cm}^2/\text{Vs})$, scattering rate $1/\tau(1/\text{ns})$, energy gap $\Delta_{5/2}(\text{mK})$ of the $\nu = 5/2$ FQHS, and $R_{5/2}^{150\text{mK}}(\Omega)$ of the measured samples.

x	n	μ	$1/\tau$	$\Delta_{5/2}$	$R_{5/2}^{150\text{mK}}$
0	3.08	20	1.3	569	27
0.00057	2.91	6.5	4.0	543	48
0.00075	2.88	5.0	5.2	360	83
0.0015	2.90	3.6	7.3	347	131
0.0026	2.70	2.7	9.7	199	209
0.0036	3.08	2.2	12	127	198
0.0046	2.82	1.7	15	-	-

slowly cooled to 5 K over 2 hours, after which we proceed to condensing the He^3-He^4 mixture. Once most of the mixture is condensed, we start filling our He^3 immersion cell.

We note that MBE-controlled alloy disorder was first introduced to 2DEGs in Ref. [100]. However, in these samples [76, 100, 101] the $\nu = 5/2$ FQHS has not been observed. In contrast, our samples have several essential features which are optimized for a strong $\nu = 5/2$ FQHS even in the presence of the disorder. First, the 2DEG is confined to a symmetrically doped quantum well rather than a single heterointerface. This allows for a higher electron density, enhancing therefore fragile FQHSs. Second, we use a reduced Al content 0.24 in the $Al_{0.24}Ga_{0.76}As$ barriers, which enhances the $\nu = 5/2$ FQHS [25, 81, 102]. Third, we use a short period superlattice doping scheme [103], which is known to yield a strong $\nu = 5/2$ FQHS [38, 79, 102].

It is important to appreciate that only the alloy disorder is different in each sample. All other sample parameters, however, are left virtually unchanged. In order to avoid any density dependent effects the electron density is kept constant, close to $n \simeq 2.9 \times 10^{11}/cm^2$. Specifically, in our samples $2.70 \times 10^{11}/cm^2 \leq n \leq 3.08 \times 10^{11}/cm^2$. Furthermore, the alloy content x of the electron channel $Al_xGa_{1-x}As$ is low when compared to that in the confining $Al_{0.24}Ga_{0.76}As$. There is therefore virtually no variation of the electronic effective mass m and of the electronic confinement in the direction perpendicular to the plane of the 2DEG [104]. Other parameters held constant include the position of the 2DEG relative to the sample surface and the thickness of the capping layer [105].

Fig 6.1 shows the magnetoresistance R_{xx} and the Hall resistance R_{xy} of the alloy-free reference sample, i.e. for which $x = 0$, measured at $T = 7$ mK in a van der Pauw geometry. The figure is limited to magnetic fields B for which the filling factor ranges between $2 < \nu < 3$, commonly referred to as the lower spin branch of the second Landau level. Because of the high quality growth and sample design described earlier we observe strong FQHSs at $\nu = 5/2$, 2+1/3, and 2+2/3 as indicated by vanishing R_{xx} and quantized R_{xy} [8, 106]. Other more fragile FQHSs are also seen in Fig.1 [36, 45].
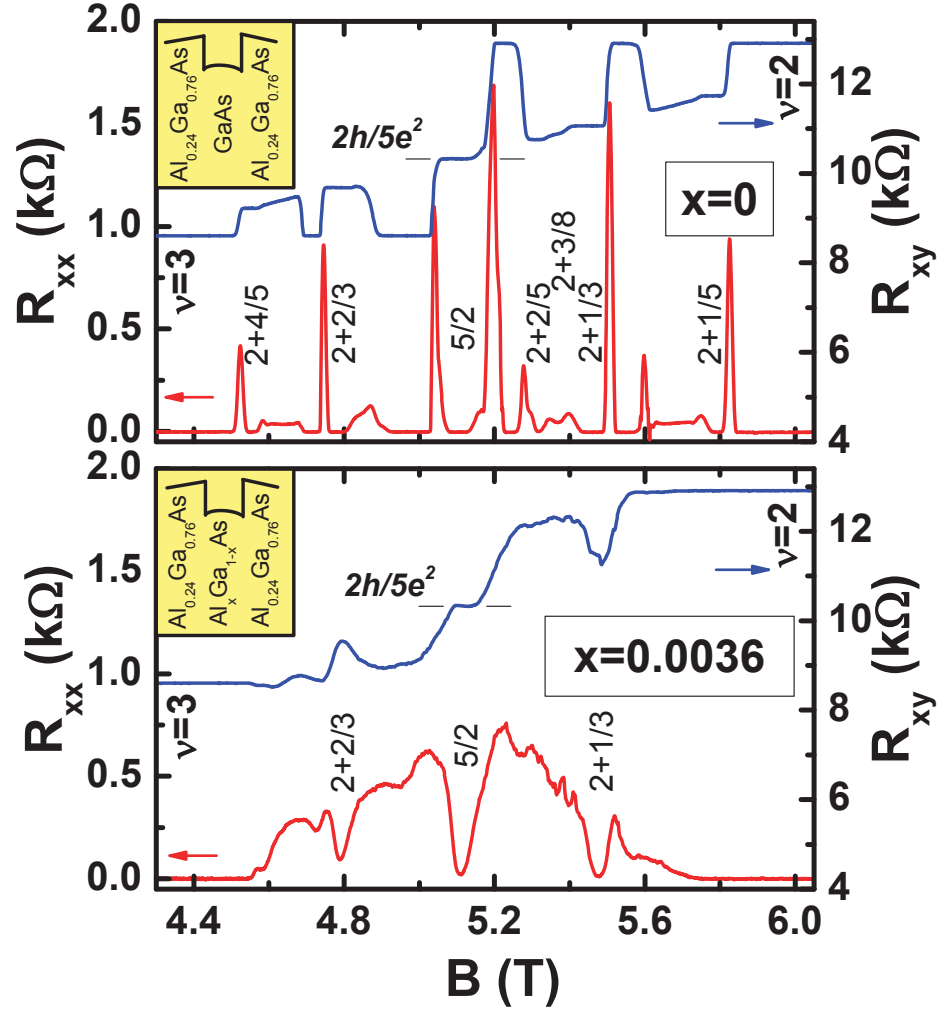
Figure 6.1. Magnetoresistance R_{xx} and Hall resistance R_{xy} in the reference sample with $x = 0$ (top panel) and the alloy sample with $x = 0.0036$ (bottom panel) as measured at 7 mK. Numbers indicate the filling factors of various FQHSs and insets are sketches of the sample structure. This data is published in Ref. [115]

Alloy disorder strongly affects magnetoresistance. This can be seen in the traces of the sample with $x = 0.0036$ gathered at 7 mK, which are also shown in Fig.1. The most fragile FQHSs, such as the $\nu = 2 + 2/5$, $2 + 1/5$, and $2 + 4/5$ FQHSs, are destroyed. The FQHS at $\nu = 5/2$, however, remains fully quantized in spite of

the presence of alloy disorder. Indeed, at this ν there is a vanishing R_{xx} and the rigorously quantized $R_{xy} = 2h/5e^2$, which holds to a precision of 1 part in 10^3.

6.2 Activated Temperature Dependence In Alloy Samples

Next we have investigated the temperature dependence of the $\nu = 5/2$ FQHS. Thermalization of electrons in our experiment is assured by the use of a ^{3}He immersion cell [35, 41] and temperature measurements of the ^{3}He bath below 100 mK are performed with the aid of a tuning fork viscosity thermometer [41]. At the lowest temperatures T the magnetoresistance of the $\nu = 5/2$ FQHS follows an activated form $R_{xx} \propto \exp(-\Delta_{5/2}/2T)$, from which we extract the energy gap $\Delta_{5/2}$. The Fig 6.2 shows the temperature dependence of R_{xx} at $\nu = 5/2$ on an Arrhenius plot, i.e. $\ln R_{xx}$ as function of $1/T$. The presence of the linear segment indicates that transport is activated. In the alloy-free reference sample we find a record high energy gap $\Delta_{5/2} = 569$ mK [36].

The Fig 6.2 also shows the T-dependence of R_{xx} at $\nu = 5/2$ in two representative alloy samples with $x = 0.00075$ and $x = 0.0036$. The presence of linear segments at non-zero x means the survival of activated transport even in the presence of alloy disorder. It is, therefore, meaningful to extract energy gaps in the alloy samples as well. Values found are summarized in Table 6.1 and are plotted as function of x in Fig 6.3. We find the $\Delta_{5/2}$ has a decreasing trend with an increasing x. At the largest value of $x = 0.0046$ we studied, we no longer observe a FQHS at $\nu = 5/2$. A linear fit to the data passing through the point associated with the $x = 0$ reference sample shows that the gap closes at the extrapolated value of $x \simeq 0.0042$. We note that the error in $\Delta_{5/2}$ as determined from the Arrhenius fits is estimated to $\pm 10\%$. However, in Fig.2 there is also scatter in the data possibly caused by small variations in the sample densities and slight variations from the target value of the alloy content x.
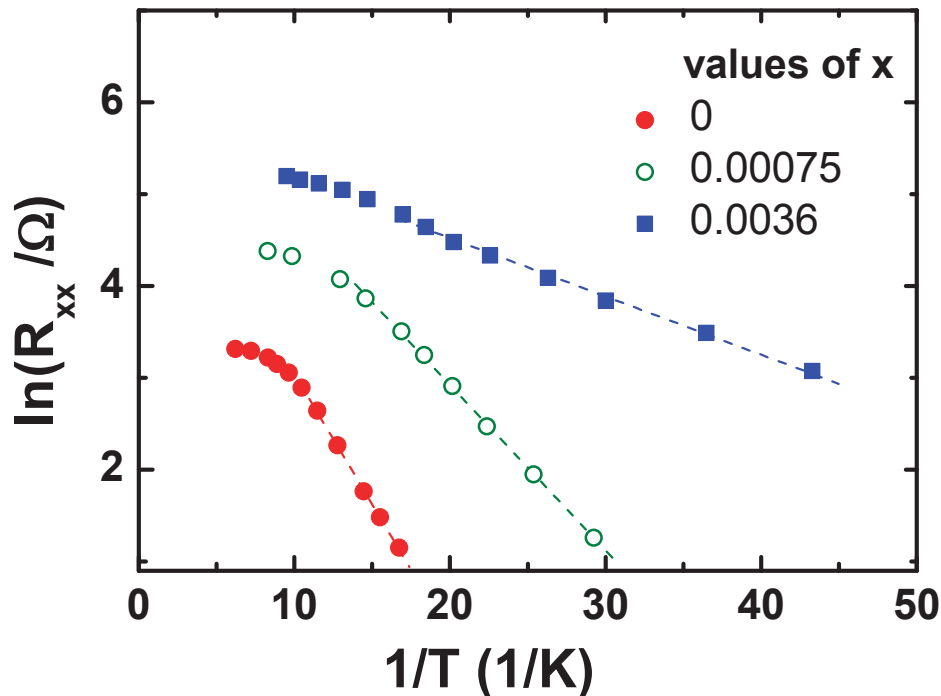
Figure 6.2. The Arrhenius plots for the $\nu = 5/2$ FQHS in three representative samples. This data is published in Ref. [115]

6.3 Impact Of Alloy Disorder On The Energy Gap Of The $\nu = 5/2$ State

The aluminum fraction x in our alloy samples is clearly a measure of the added disorder. In the literature the most commonly used metric for the disorder is the mobility μ. Early work on the $\nu = 5/2$ FQHS found that the energy gap of the state correlates well with the mobility. It was found that a higher μ resulted in a larger $\Delta_{5/2}$ and the $\nu = 5/2$ FQHS does not develop for mobility less than the threshold value $\mu_C \simeq 10 \times 10^6 \mathrm{cm}^2/\mathrm{Vs}$. Later it became apparent that there is in fact a poor correlation between $\Delta_{5/2}$ and μ [81, 84]. Nonetheless, a threshold μ_C below which a $\nu = 5/2$ FQHS does not develop was still identified. The shaded area of Fig 6.4 shows the stability region of the $\nu = 5/2$ FQHS in high quality alloy-free samples at densities $2.65 \times 10^{11} \leq n \leq 3.2 \times 10^{11}/\mathrm{cm}^2$ close to that of our samples [25, 36, 39, 80, 81, 83, 84].
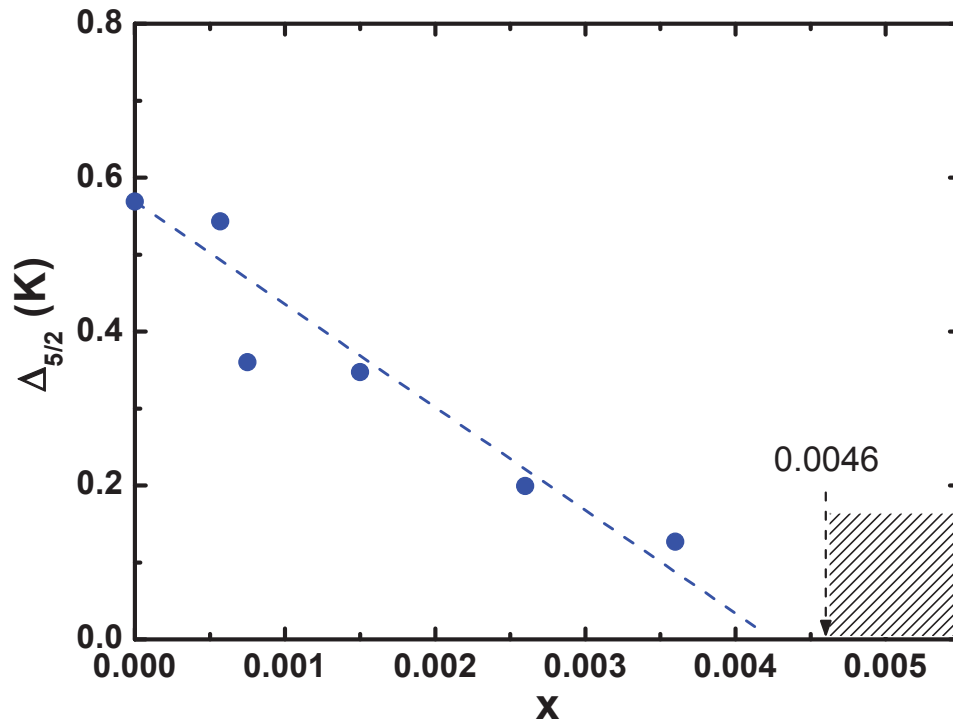
Figure 6.3. The dependence of $\Delta_{5/2}$ on the aluminum mole fraction x. In a sample with $x = 0.0046$ we do not observe a FQHS at $\nu = 5/2$, hence the excluded shaded area. This data is published in Ref. [115]

These data are taken from the literature. A threshold value $\mu_C \simeq 7 \times 10^6 \text{cm}^2/\text{Vs}$ for these alloy-free samples is clearly seen.

Fig 6.4 also shows that a strong $\nu = 5/2$ FQHS with $\Delta_{5/2} = 127$ mK develops in the alloy sample with $\mu = 2.2 \times 10^6 \text{cm}^2/\text{Vs}$. This is surprising, since at such a low mobility a $\nu = 5/2$ FQHS has never been observed. Indeed, this mobility is much below the the previously established $\mu_C \simeq 7 \times 10^6 \text{cm}^2/\text{Vs}$ threshold in high quality alloy-free samples. We thus found that the mobility threshold for a fully quantized $\nu = 5/2$ FQHS is significantly lowered in the presence of alloy disorder and, therefore, the $\nu = 5/2$ FQHS is robust to the presence of alloy disorder. Furthermore, we conclude that alloy disorder does not appear to be as detrimental to the development of the $\nu = 5/2$ FQHS as the residual disorder unintentionally added during sample

growth. The gap $\Delta_{5/2}$ for our alloy samples closes at an extrapolated new threshold of $\mu_C^{alloy} \simeq 1.8 \times 10^6 \mathrm{cm}^2/\mathrm{Vs}$.
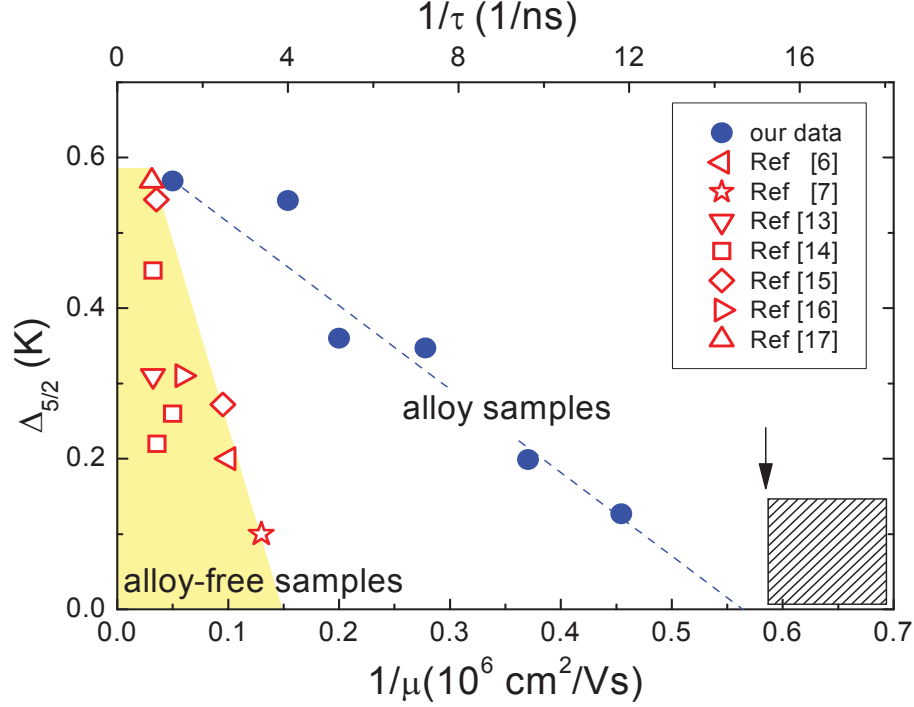
Figure 6.4. The dependence of $\Delta_{5/2}$ on inverse mobility $1/\mu$ and the electronic scattering rate $1/\tau$ of our samples (closed symbols) and of alloy-free samples from the literature with densities near $2.9 \times 10^{11}/\mathrm{cm}^2$. In our alloy samples the $\nu = 5/2$ FQHS survives at surprisingly high $1/\mu$ and, therefore, low μ. The arrow indicates a sample in which the $\nu = 5/2$ FQHS does not develop. This picture is taken from Ref. [115]

It is important to appreciate that not only our samples have controllably added alloy disorder but, with the exception of the sample with $x = 0.00057$, alloy disorder is the dominant scattering mechanism. This is the case because the electron scattering rate in our alloy samples $1/\tau$ exceeds the residual scattering rate of the alloy-free reference sample $1/\tau_{residual} = 1.3\mathrm{ns}^{-1}$ [99]. Here $\tau = \mu m/e$ is the transport scattering

time. As seen in Fig 6.3, $\Delta_{5/2}$ is linearly decreasing with $1/\tau$ with the slope of 41 mK·ns. Furthermore, we find that the gap extrapolates to zero near $1/\tau \simeq 15$ ns^{-1}.

Since Al is a neutral impurity, when added to a perfect GaAs crystal, it perturbs the crystal potential on sub-nanometer length scale. The alloy disorder we study thus generates a short-range scattering potential [100]. In a recent experiment a different type of short-range disorder, that due to surface roughness scattering, was investigated [80]. It was found that in a heterojunction insulated gate field-effect transistor $\Delta_{5/2}$ increases with a decreasing mobility, a result which is opposite to our findings. One reason for this discrepancy is that in Ref. [80] the electron density is increased as the mobility is decreasing. The quantitative effect of the disorder on the energy gap in Ref. [80], therefore, remains difficult to extract. Indeed, the dominance of the short-range scattering could not be ascertained and the gap altering effects of the combination of changing density and wavefunction confinement were not disentangled from that of the disorder [80]. In two other experiments, the effect on the $\nu = 5/2$ FQHS of a different type of disorder, that due to the remote ionized dopants was investigated [79, 81]. It was found that increasing the level of the remote dopants leads to the strengthening of the $\nu = 5/2$ FQHS [81]. A systematic dependence of the energy gap on overdoping, however, remains unavailable to date. Our results thus highlight the effect of the short-range alloy disorder on the stability of the $\nu = 5/2$ FQHS, whereas the effect of other important types of disorder, such as those of the long-range Coulomb potentials of dopants and of background impurities, remain unknown.

The lack of correlation of $\Delta_{5/2}$ and μ in alloy-free samples reported in the literature remains an outstanding puzzle [81, 84]. We propose that such a lack of correlation between $\Delta_{5/2}$ and μ appears because a) a well defined $\Delta_{5/2}$ versus μ correlation exists when only one type of disorder dominates and a single heterostructure design is employed and b) for each kind of disorder the $\Delta_{5/2}$ versus μ functional relationship is different. In other words, because high quality alloy-free samples most likely have a different mix of the various disorders and because $\Delta_{5/2}$ and μ track differently

for each specific type of disorder, the result is a lack of correlation of $\Delta_{5/2}$ and μ when an analysis of dissimilar samples is undertaken. In contrast, when in a series of similar samples one type of disorder dominates, such as in our experiment, $\Delta_{5/2}$ and μ should be correlated. We suggest that the quasi-linear correlation of $\Delta_{5/2}$ and μ in our alloy samples shown in Fig 6.3 supports the above hypothesis. This hypothesis, however, remains to be tested in instances in which various other types of disorder are dominant. A natural consequence of our analysis is that μ measured at zero B-field, and the single-particle lifetime measured in the low B-field semi-classical regime [107] are poor measures of the impact of the disorder on many-body ground states developed at large B-fields [38, 79–81]. We note that we have measured the single-particle lifetime τ_q for our series of samples and found no obvious correlation with $\Delta_{5/2}$.

6.4 Correlating Low Temperature Resistivity With The Energy Gap Of The $\nu = 5/2$ State

As seen in the Fig 6.2, above 100 mK there is little or no change with temperature in the magnetoresistance R_{xx} at $\nu = 5/2$. According to the CF description, in this regime the system is described by a Fermi sea of the CFs in a zero effective magnetic field [5,108]. We find the temperature-independent R_{xx} value above 100 mK correlates with the amount of disorder. The values of $R_{5/2}^{150\text{mK}}$, the saturation value of R_{xx} at 150 mK measured at $\nu = 5/2$, are listed in the Table 6.1. We notice that, $R_{5/2}^{150\text{mK}}$ increases with an increasing x. According to the CF theory, $R_{5/2}^{150\text{mK}}$ is a measure of the scattering of the CF with the impurities [5,108–110]. We conclude that the linear increase of $R_{5/2}^{150\text{mK}}$ with x is a direct consequence of enhanced scattering rate of the CFs as x increases. We thus find that at $\nu = 5/2$ an increasing alloy disorder has two independent concurring effects: it reduces the energy gap of the state and it enhances $R_{5/2}^{150\text{mK}}$, the T-independent R_{xx} at $\nu = 5/2$ in the limit of high temperatures.

In an effort to speed up the screening of the samples and to characterize them at ^{3}He refrigerator temperatures at which the $\nu = 5/2$ FQHS does not yet develop, it was proposed that strong $\nu = 5/2$ FQHSs develop in samples with low values of the T-independent R_{xx} measured at $\nu = 5/2$ [38]. We thus found that such a hypothesis has a natural explanation within the framework of the composite fermion theory and, furthermore, that the hypothesis works in samples with alloy disorder. This hypothesis, however, remains to be further tested in samples with different types of dominating disorder.

We note that recently an alternative method of extracting the energy gap has been proposed [111]. This model, however, is formulated for the slowly varying potential generated by the remote dopants and it yet remains to be extended to alloy scattering. There is also effort in understanding short-range scatterers, albeit so far only for the $\nu = 1/3$ FQHS [112].

6.5   Conclusions

In conclusion, I study the effect of alloy disorder on the $\nu = 5/2$ FQHS in a regime in which alloy disorder dominates. The gap of the $\nu = 5/2$ FQHS closes at unprecedentedly low mobility which indicates that alloy disorder may not be as detrimental to the formation of the $\nu = 5/2$ FQHS as other types of disorder. Our quantitative results will be useful in understanding the nature of the $\nu = 5/2$ FQHS and in engineering a stronger $\nu = 5/2$ FQHS.

LIST OF REFERENCES

LIST OF REFERENCES

[1] K. von Klitzing, G. Dorda, and M. Pepper, Phys. Rev. Lett. **45**, 494 (1980).

[2] John H. Davies, "The Physics of Low-Dimensional Semiconductors", Cambridge University press, 1998.

[3] D.C. Tsui, H.L. Stormer, and A.C. Gossard, Phys. Rev. Lett. **48**, 1559 (1982).

[4] R.B. Laughlin, Phys. Rev. Lett. **50**, 1395 (1983).

[5] J.K. Jain, Phys. Rev. Lett. **63**, 199 (1989).

[6] Jainendra K. Jain, "Composite Fermions", Cambridge University press, 2007.

[7] R.R. Du *et al.*, Phys. Rev. Lett. **70**, 2944 (1993); R.R. Du *et al.*, Phys. Rev. Lett. **75**, 3926 (1995); F. Schulze-Wischeler *et al.*, Phys. Rev. Lett. **92**, 156401 (2004);

[8] R. Willett *et al.*, Phys. Rev. Lett. **59**, 1776 (1987).

[9] G. Moore and N. Read, Nucl. Phys. B **360**, 362 (1991).

[10] M. Greiter, X.G. Wen, and F. Wilczek, Phys. Rev. Lett. **66**, 3205 (1991).

[11] C. Nayak and F. Wilczek, Nucl. Phys. B 479, 529 (1996).

[12] P. Bonderson, V. Gurarie, C. Nayak, Phys. Rev. Lett. **83**, 075303 (2011).

[13] K. Park, V. Melik-Alaverdian, N.E. Bonesteel, and J.K. Jain, Phys. Rev. B. **58**, R10167 (1998).

[14] N. Read, and E. Rezayi, Phys. Rev. B. **59**, 8084 (1999).

[15] V. Scarola, K. Park, and J.K. Jain, Nature (London) **406**, 863 (2000).

[16] E.H. Rezayi and F.D.M. Haldane, Phys. Rev. Lett. **84**, 4685 (2000).

[17] N. Read and D. Green, Phys. Rev. B. **61**, 10267 (2000).

[18] H. Lu, S. Das Sarma, and K. Park, Phys. Rev. B. **82**, R201303 (2010).

[19] S. Das Sarma, M. Freedman, and C. Nayak, Phys. Rev. Lett. **94**, 166802 (2005).

[20] R.L. Willett *et al.*, Phys. Rev. B **38**, 7881 (1988).

[21] R.L. Willett *et al.*, Phys. Rev. B **38**, 7881 (1988); E.Y. Andrei *et al.*, Phys. Rev. Lett. **60**, 2765 (1988); V.J. Goldman, M. Shayegan, and D.C. Tsui, Phys. Rev. Lett. **61**, 881 (1988); V.J. Goldman et al., Phys. Rev. Lett. **65**, 2189 (1990); F.I.B. Williams *et al.*, Phys. Rev. Lett. **66**, 3285 (1991); L.W. Engel et al., Solid State Commun. **104**, 167 (1997); P.D. Ye *et al.*, Phys. Rev. Lett. **89**, 176802 (2002); B.A. Piot *et al.*, Nat. Phys. **4**, 936 (2008).

[22] A.A. Koulakov, M.M. Fogler, and B.I. Shklovskii, Phys. Rev. Lett. **76**, 499 (1996).

[23] M.P. Lilly *et al.*, Phys. Rev. Lett. **82**, 394 (1999).

[24] R.R. Du *et al.*, Solid State Commun. **109**, 389 (1999).

[25] J.P. Eisenstein *et al.*, Phys. Rev. Lett. **88**, 076801 (2002).

[26] P.W. Anderson, Phys. Rev. **109**, 1492 (1958).

[27] F.D.M. Haldane, E.H. Rezayi, and K. Yang, Phys. Rev. Lett. **85**, 5396 (2000).

[28] N.Shibata and D. Yoshioka, Phys. Rev. Lett. **86**, 5755 (2001).

[29] M.O. Goerbig, P. Lederer, and C.M. Smith, Phys. Rev. B **68**, 241302 (2003); **69**, 115327 (2004).

[30] K.B. Cooper *et al.*, Phys. Rev. B **60**, 11285 (1999).

[31] R.M. Lewis *et al.*, Phys. Rev. Lett. **89**, 136804 (2002).

[32] R.M. Lewis *et al.*, Phys. Rev. Lett. **93**, 176808 (2004).

[33] R.M. Lewis *et al.*, Phys. Rev. B **71**, 081301 (2005).

[34] T. Lin *et al.*, arXiv:1311.2954 (2013).

[35] W. Pan, J.S. Xia, V. Shvarts, D.E. Adams, H.L. Stormer, D.C. Tsui, L.N. Pfeiffer, K.W. Baldwin, and K.W. West, Phys. Rev. Lett. **83**, 3530 (1999).

[36] A. Kumar *et al.*, Phys. Rev. Lett. **105**, 246808 (2010).

[37] L.N. Pfeiffer and K.W. West, Physica E **20**, 57 (2003).

[38] M.J. Manfra, arXiv:1309.2717.

[39] W. Pan *et al.*, Phys. Rev. B **77**, 075307 (2008).

[40] F. Pobell, "Matter and methods at low temperatures", 3rd ed., Springer 2007.

[41] N. Samkharadze *et al.* Rev. Sci. Instr. **82**, 053902 (2011).

[42] W.C. Black, W.R. Roach and J.C. Wheatley, Rev. Sci. Instr. **35**, 587 (1964).

[43] Operator's Handbook of Oxford Instruments [43]

[44] F. Fischer and M. Grayson, J. Appl. Phys. **98**, 013710 (2005).

[45] J.S. Xia, *et al.* Phys. Rev. Lett. **93**, 176809 (2004).

[46] N. Shibata and D. Yoshioka, J. Phys. Soc. Jpn. **72**, 664 (2003).

[47] I.P. Radu *et al.*, Science **320**, 899 (2008).

[48] M. Dolev *et al.*, Phys. Rev. Lett. **107**, 036805 (2011).

[49] N. Samkharadze *et al.*, Phys. Rev. B. **84**, R121305 (2011).

[50] G.A. Csáthy *et al.*, Phys. Rev. Lett. **94**, 146801 (2005).

[51] C.R. Dean *et al.*, Phys. Rev. Lett. **100**, 146803 (2008).

[52] V. Umansky *et al.* J. Crystal Growth **311**, 1658 (2009).

[53] J. Nuebler *et al.*, Phys. Rev. B. **81**, 035316 (2010).

[54] J. Xia *et al.*, Phys. Rev. Lett. **105**, 176807 (2010).

[55] M. Levin, B.I. Halperin, and B. Rosenow, Phys. Rev. Lett. **99**, 236806 (2007).

[56] S.S. Lee *et al.*, Phys. Rev. Lett. **99**, 236807 (2007).

[57] X. Wan *et al.*, Phys. Rev. B. **77**, 165316 (2008).

[58] H. Wang, D.N. Sheng, and F.D.M. Haldane, Phys. Rev. B. **80**, 241311 (2009).

[59] W. Bishara and C. Nayak, Phys. Rev. B. **80**, 121302 (2009).

[60] M.R. Peterson, K. Park, and S. Das Sarma, Phys. Rev. Lett. **101**, 156803 (2008).

[61] A. Wójs, C. Toke, and J.K. Jain, Phys. Rev. Lett. **105**, 096802 (2010).

[62] E.H. Rezayi and S.H. Simon, Phys. Rev. Lett. **106**, 116801 (2011).

[63] M.M. Fogler, and A.A. Koulakov, Phys. Rev. B. **55**, 9326 (1997).

[64] M.M. Fogler, in "High Magnetic Fields: Applications in Condensed Matter Physics and Spectroscopy", edited by C. Berthier, L.P. Lévy, and G. Martinez, Springer-Verlag, 2002

[65] R. Côté *et al.* Phys. Rev. B **68**, 155327 (2003); R. Côté *et al.* Phys. Rev. B **72**, 115344 (2005).

[66] R. Moessner and J.T. Chalker, Phys. Rev. B **54**, 5006 (1996).

[67] H. Fukuyama, P.M. Platzman, and P.W. Anderson, Phys. Rev. B **19**, 5211 (1979).

[68] Y. Liu et al., Phys. Rev. Lett. 109, 036801 (2012).

[69] E. H. Rezayi and F. D. M. Haldane, Phys. Rev. B **42**, 4532 (1990);

[70] A. Wójs and J. J. Quinn, Phys. Rev. B **74**, 235319 (2006);

[71] K.B. Cooper *et al.*, Phys. Rev. Lett. **92**, 026806 (2004).

[72] G. Gervais *et al.*, Phys. Rev. Lett. **93**, 266804 (2004).

[73] I. L. Aleiner and L. I. Glazman, Phys. Rev. B **52**, 11296 (1995).

[74] W. E. Chickering *et al.*, Phys. Rev. B **87**, 075302 (2013).

[75] E.H. Hwang and S. Das Sarma, Phys. Rev. B **77**, 235437 (2008)

[76] W. Li *et al.*, Phys. Rev. Lett. **94**, 206807 (2005); W. Li *et al.*, Phys. Rev. Lett. **102**, 216801 (2009).

[77] L.A. Wray *et al.*, Nature Physics. **7**, 32 (2011).

[78] J. Billy *et al.*, Nature Physics. **453**, 891 (2008); G. Roati *et al.*, Nature Physics. **453**, 895 (2008).

[79] V. Umansky *et al.*, J. Cryst. Growth. **311**, 1658 (2009).

[80] W. Pan *et al.*, Phys. Rev. Lett. **106**, 206806 (2011).

[81] G. Gamez and K. Muraki, Phys. Rev. B. **88**, 075308 (2013).

[82] B.E. Feldman, B. Krauss, J.H. Smet, and A. Yacoby, Science 337, 1196 (2012).

[83] H.C. Choi *et al.*, Phys. Rev. B. **77**, 081301 (2008).

[84] J. Nuebler *et al.*, Phys. Rev. B. **81**, 035316 (2010).

[85] Yang Liu *et al.*, Phys. Rev. Lett. **107**, 176805 (2011).

[86] Guangtong Liu *et al.*, Phys. Rev. Lett. **108**, 196805 (2012).

[87] U. Wurstbauer, K.W. West, L.N. Pfeiffer, and A. Pinczuk, Phys. Rev. Lett. **110**, 026801 (2013)

[88] M. Dolev *et al.*, Nature. **452**, 829 (2008).

[89] A. Bid *et al.*, Nature. **466**, 585 (2010).

[90] R.L. Willett, L.N. Pfeiffer, and K.W. West, Phys. Rev. B. **82**, 205301 (2010).

[91] V. Venkatachalam, A. Yacoby, L. Pfeiffer, and K. West, Nature **469**, 185 (2011).

[92] A.P. MacKenzie and Y. Maeno, Rev. Mod. Phys. **75**, 657 (2003).

[93] J. Sau, R.M. Lutchin, S. Tewari, and S. Das Sarma, Phys. Rev. Lett. **104**, 040502 (2010); J. Alicea, Phys. Rev. B **81**, 125318 (2010).

[94] A.J. Leggett, Rev. Mod. Phys. **47**, 331 (2003).

[95] A.C. Clark *et al.* , Rev. Sci. Instr. **81**, 103904 (2010).

[96] R.H. Morf, N. d'Ambrumenil, and S. Das Sarma, Phys. Rev. B. **66**, 075408 (2002).

[97] R. Morf and N. d'Ambrumenil, Phys. Rev. B. **68**, 113309 (2003).

[98] A.E. Feiguin, E. Rezayi, C. Nayak, and S. Das Sarma, Phys. Rev. Lett. 100, 166803 (2008).

[99] G.C. Gardner *et al.*, Appl. Phys. Lett. **102**, 252103 (2013).

[100] W. Li *et al.*, Appl. Phys. Lett. **83**, 2832 (2003).

[101] W. Li *et al.*, Phys. Rev. Lett. **105**, 076803 (2010).

[102] L.N. Pfeiffer, private communication.

[103] K.J. Friedland, R. Hey, H. Kostial, R. Klann, and K. Ploog, Phys. Rev. Lett. **77**, 4616 (1996).

[104] we used the software NextNano3, from the Walter Schottky Institute.

[105] Laroche at al, Appl. Phys. Lett. **96**, 162112 (2010).

[106] H.L. Stormer, D.C. Tsui, and A.C. Gossard, Rev. Mod. Phys. **71**, 298 (1999).

[107] P.T. Coleridge, Phys. Rev. B **44**, 3793 (1991).

[108] B.I. Halperin, P.A. Lee, and N. Read, Phys. Rev. B **47**, 7312 (1993).

[109] W. Kang *et al.*, Phys. Rev. Lett. **75**, 4106 (1995).

[110] J. Zhang, R.R. Du, J.A. Simmons, and J.L. Reno, Phys. Rev. B. **81**, 041308(R) (2010).

[111] N. d'Ambrumenil, B.I. Halperin, and R.H. Morf, Phys. Rev. Lett. **106**, 126804 (2011).

[112] D.N. Sheng *et al.*, Phys. Rev. Lett. **90**, 256802 (2003).

[113] N. Deng *et al.*, Phys. Rev. Lett. **108**, 086803 (2012).

[114] N. Deng *et al.*, Phys. Rev. B. **86**, 201301(R) (2012).

[115] N. Deng *et al.*, Phys. Rev. Lett. **112**, 116804 (2014).

[116] N. Deng *et al.*, manuscript in preparation.

[117] E. Kleinbaum *et al.*, arXiv:1410.6571 (2014).

VITA

VITA

Personal Information

Nianpei Deng was born in Wuhan, Hubei, China and earned his Bachelor of Science degree in Physics in Peking University. After graduation with Bachelor of Science degree in 2010, he joined the graduate school of Purdue University and worked as a research assistant in the fields of ultra-low temperature condensed matter experiments.

Education

Purdue University, West Lafayette, Indiana, USA
Ph.D. Candidate, Physics. Advisor: G.A. Csáthy Dissertation Title: "Transport Studies of Reentrant Integer Quantum Hall States Forming in The Two-dimensional Electron Gas"

Peking University, Beijing, China
B.S., Physics, June 2010.